A STUDY OF THE VISCOUS INTERACTION BETWEEN THE SOLAR WIND AND EARTH'S MAGNETOSPHERE USING AN MHD SIMULATION

by

ROBERT JEFFREY BRUNTZ

Presented to the Faculty of the Graduate School of
The University of Texas at Arlington in Partial Fulfillment
of the Requirements
for the Degree of

DOCTOR OF PHILOSOPHY

THE UNIVERSITY OF TEXAS AT ARLINGTON

May 2012

ACKNOWLEDGEMENTS

I would like to thank my family for their constant support - my parents, my sister, brother-in-law, niece, nephew, and grandfather - as well as the many friends who have encouraged and accompanied me along the way. A few in particular: Betsey, Ximena, Rodney, Sandra, Bruce, Emrys, Shree, Kevin, and Paul (but also many others - you know who you are).

Numerous colleagues have contributed material to this research and/or to my development as a scientist, including Dr. Michael Wiltberger, Dr. John Lyon, Dr. Yue Deng, Dr. Elizabeth Mitchell, Shree Bhattarai, Kevin Pham, Yanshi Huang, Pete Schmitt, and many faculty and staff at the University of Texas at El Paso, the Florida Institute of Technology, and the University of Texas at Arlington. (They tried their best, so they shouldn’t be blamed for any flaws I still retain.)

I would also like to express my appreciation to my graduate committee: Drs. Yue Deng, Ali Koymen, Samarendra Mohanty, and Sangwook Park.

Finally, I would like to express my appreciation and admiration for my graduate advisor, Dr. Ramon E. Lopez, who I believe fits into each section above. It has been an honor to be, in overlapping time periods, an employee and student under Ray, and I have learned more from him than I could fit into a hundred dissertations. (I don't think they would all be publishable anyway, since most people would not be able to repeat what he has done - not the least of which is seeing me through to this graduation.) I also appreciate his family (especially Ellen), which has become a family-away-from-home for me.

Some say that money makes the world go around; though we actually know that it's angular momentum. Nevertheless, here are some funding sources that have helped keep us busy over the last several orbits:

This material is based upon work supported by CISM, which is funded by the STC Program of the National Science Foundation under Agreement Number ATM-0120950.

The National Center for Atmospheric Research (funding M. Wiltberger) is sponsored by the National Science Foundation.

Y. Deng’s effort at the University of Texas at Arlington was supported by the Nation Science Foundation under ATM0955629.

And of course, always, to the Creator of such an interesting universe.

"These are but the outer fringe of his works; how faint the whisper we hear of him! Who then can understand the thunder of his power?"   - Job 26:14

April 17, 2012

ABSTRACT

A STUDY OF THE VISCOUS INTERACTION BETWEEN THE SOLAR WIND AND EARTH'S MAGNETOSPHERE USING AN MHD SIMULATION

Robert Jeffrey Bruntz, PhD

The University of Texas at Arlington, 2012

Supervising Professor: Ramon E. Lopez

The solar wind interacts with Earth's magnetosphere largely through magnetic reconnection and a "viscous-like" interaction that is not fully understood. The ionospheric cross-polar cap potential (Φ_{PC}) component due to reconnection (Φ_R) is typically much larger than the viscous component (Φ_V) and very dynamic, making detailed studies of the viscous potential difficult. We used the Lyon-Fedder-Mobarry (LFM) magnetohydrodynamic (MHD) simulation to study the viscous potential by running LFM for a variety of solar wind density and velocity values and ionospheric Pedersen conductance (Σ_P) values, but no solar wind magnetic field, so that Φ_{PC} was entirely due to the viscous interaction. We found that Φ_V increased with solar wind

density, scaling as $n^{0.439}$ (n in cm^{-3}), and Φ_V increased with solar wind velocity, scaling as $V^{1.33}$ (V in km s^{-1}); these results were combined to create a formula for Φ_V in LFM, using a Σ_P value that produces realistic potentials: $\Phi_V = (0.00431)n^{0.439}V^{1.33}$ (in kV), which matches simulation results very well. Φ_V also varied inversely with Σ_P, as predicted by previous theory. The form of this formula is similar to results from the *Newell et al.* [2008] empirical study, which tested a list of viscous coupling functions and found that $n^{1/2}V^2$ worked best (but did not create a formula to predict potentials, so actual viscous potential values could not be compared).

The Bruntz et al. formula was also compared to LFM results from a run with real solar wind input, from the Whole Heliosphere Interval (WHI), which lasted from 20 March to 16 April 2008. LFM was first run with the full solar wind from the WHI, then with the same solar wind but zero interplanetary magnetic field (IMF), which meant that $\Phi_{PC} = \Phi_V$ for that run. These runs were performed with the empirical ionospheric solver, using the average F10.7 flux value from the WHI as input. This empirical ionosphere is known to produce potentials that are higher than observations, so the output was scaled down to match the range of the Bruntz et al. formula with a scaling factor $\gamma = 1.542$, which was found from 11 steady periods in the WHI. Those same periods were also used to calibrate the Newell et al. viscous scaling factor, turning it into a predictive formula: $\Phi_V = (6.39\times10^{-5})n^{1/2}V^2$ (in kV). Both viscous potential formulas were compared to Φ_{PC} from the zero-IMF run, producing Φ_V values that were very close to the LFM Φ_{PC} values, differing in opposite ways in some places, but with essentially identical correlation coefficients.

We also used the γ factor to scale Φ_{PC} from the full-IMF LFM run down, then compared it to Φ_{PC} from the Weimer05 empirical model. The two matched well in the higher Φ_{PC} values, but the Weimer05 Φ_{PC} values reached a minimum "floor" value, while the LFM Φ_{PC} has no such floor, and so dropped much lower in some places. The fact that γ scaled the full-IMF LFM down to match the Weimer05 values, even though γ was derived from very different runs and conditions, is interpreted to support the idea that the cause of high LFM potentials is in the ionospheric conductivity, since γ is derived from the higher-conductivity-based Bruntz et al. formula.

TABLE OF CONTENTS

LIST OF ILLUSTRATIONS

Figure Page

LIST OF TABLES

Table Page

CHAPTER 1

INTRODUCTION

1.1 The Sun and solar wind

Just like weather on Earth, space weather is constantly occurring above our heads and around us in all directions. It is generally invisible to the naked eye, but not necessarily without consequences for life on Earth. This dissertation looks at a very small slice of space weather – the interaction between Earth and some of the mass and energy emitted by the Sun. This sliver, the viscous interaction, is generally just a whisper in the maelstrom swirling and flowing around Earth; but sometimes it's more than a whisper.

1.1.1 The Sun's energy - the driver of space weather

The Sun is the ultimate source of almost all space weather in our solar system. Nuclear fusion in the Sun's core provides the energy to keep the Sun's surface (the photosphere) at a steady-state temperature of approximately 6,000 K (Figure 1-1). A few thousand kilometers farther out, though, through processes that are not yet fully understood, the temperature of the Sun's atmosphere rises to the range of 1,000,000 K. This superheated plasma is nearly completely ionized for all elements that comprise it and forms the basis of the solar wind, which flows out from the Sun in all directions throughout the solar system, continuously though not uniformly.

The Sun generates its own magnetic field. Since the Sun is made almost entirely of plasma, in which almost every atom has had at least some of its electrons separated from it, the solar atmosphere and magnetic field interact. The plasma can move parallel to magnetic field lines easily, but due to its high electrical conductivity, it cannot easily move perpendicular to magnetic field lines, with the plasma instead gyrating around the field line, due to the Lorentz force. In plasma physics, this is known as "frozen-in flux," meaning that the magnetic field and the plasma are frozen together (at least on the timescales we typically care about). The ratio of thermal pressure to magnetic pressure, commonly referred to as the plasma's "beta," $\beta = nkT/(B^2/2\mu_0)$, determines whether the plasma motion moves the magnetic field with it ($\beta >> 1$), the magnetic field constrains which directions the plasma can go ($\beta << 1$), or something in between ($\beta \sim 1$). Near the surface of the Sun, the magnetic pressure dominates, typically guiding the motion of the plasma, but in the much hotter plasma of the corona, the thermal pressure dominates, and so the plasma drags the magnetic field with it as it flows out into the solar system.

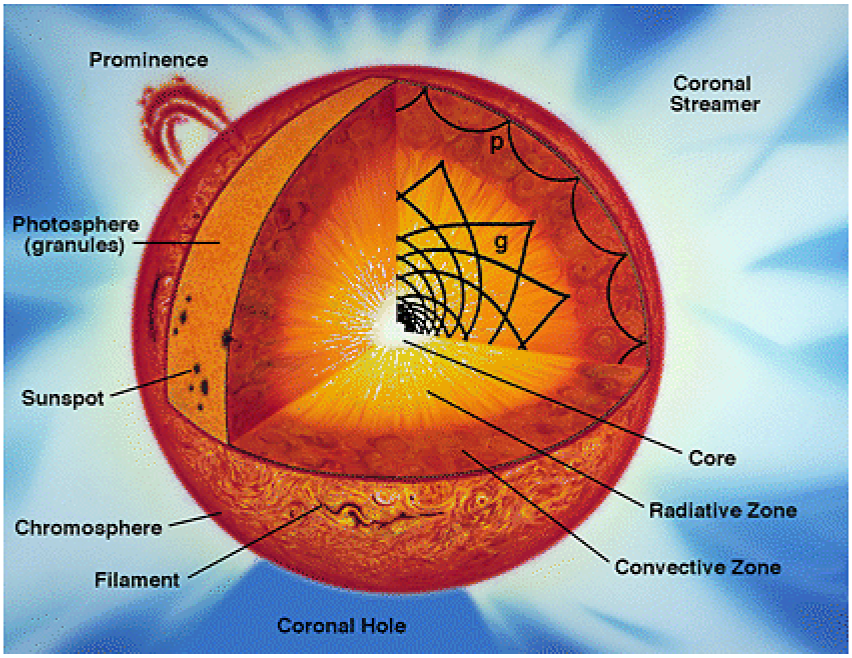

Figure 1-1. Structure of the Sun and solar atmosphere.
[Image source: NSO/GONG.]

1.1.2 Typical characteristics of the solar wind and typical ranges

The solar wind tends to have different characteristics near the Sun's poles versus its equatorial plane, which is angled about 7° off from the plane of the ecliptic and Earth's orbit. The solar wind that reaches Earth is typically moving at around 400 km/s, though it will sometimes drop down to the range of 300 km/s, and on occasion rise to the range of 1000 km/s. The average density is about 5 particles per cubic centimeter (#/cc), but can fluctuate quickly and by several orders of magnitude – dropping well below 1/cc or up into the 10's of particles per cm^3. The dominant ion species is hydrogen, at about 95% (by particle count, not mass), with around 4% helium, and traces of other elements. The plasma temperature is typically around 100,000-300,000 K, depending on particle species. The typical sound speed (a compressional wave) in the solar wind is around 60 km/s – thus, the solar wind's flow past the Earth is highly supersonic. All of these values [*Kivelson and Russell*, 1995; *Kallenrode*, 2004] are averages for typical, steady-state conditions; extreme conditions, of course, can produce much higher or lower values.

The magnetic field in the solar wind, also known as the interplanetary magnetic field or IMF, varies greatly in both magnitude and direction. Typical magnitude is around 5 nT, but the direction is highly variable. The direction is very important, as will be discussed later, since the component of the field parallel to Earth's magnetic dipole axis has a strong effect on the rate at which energy is transferred from the solar wind to Earth and its surroundings.

One common coordinate system used in magnetospheric physics the Geocentric Solar Magnetospheric (GSM) system. In this coordinate system, the x-axis points from the center of the Earth to the center of the Sun; the z-axis is in a plane defined by the x-axis and the Earth's magnetic dipole axis, with positive z pointing in the same sense as the south magnetic pole (which is about 11° displaced from the north geographic pole), and the y-axis completes a right-hand system. This coordinate system thus makes a small rotation around the x-axis every 24 hours, as the magnetic pole rotates with the Earth around the rotational axis. There is also an annual variation, as the Earth orbits the Sun and so the rotational axis changes its orientation to the Sun. One major benefit of using this coordinate system is that it lines Earth's magnetic dipole up with the z-axis of the IMF, which will be important in the discussion of solar wind-magnetosphere interaction.

1.2 Earth's magnetosphere

1.2.1 Earth's dipole; modification of shape by flow of solar wind

The Earth's magnetic field can be approximated as a dipole, and for a few R_E (1 R_E = 1 Earth radius ≈ 6371 km), that geometry describes the field well. Farther out, however, the flow of the solar wind distorts and confines Earth's magnetic field. This "bubble" in the solar wind is called Earth's magnetosphere, inside which the magnetic field and plasma are dominated by Earth's influence, and outside of which the magnetic field and plasma are dominated by the solar wind (Figure 1-2).

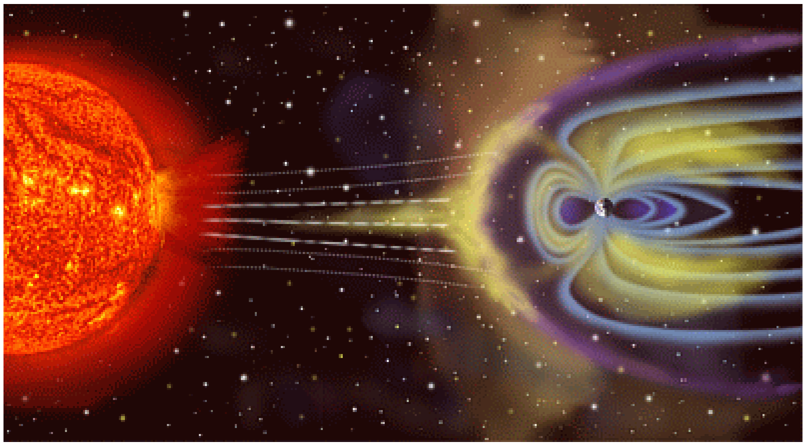

Figure 1-2. Solar wind flowing around Earth's magnetosphere (not to scale).
[Source: NASA/SEC.]

When the solar wind reaches Earth, its speed relative to the Earth is almost always greater than the fastest wave that can propagate through it. Thus, the information that there is an obstacle to go around (Earth's magnetosphere) cannot be transmitted upstream, and so a shockwave must form (Figure 1-3). The sunward edge, the bow shock, transitions the solar wind into a region in which the flow speed is decreased and the wave speed is increased, allowing information to propagate throughout the shocked region, the magnetosheath. This allows for diversion of the magnetosheath plasma, which is still entirely of solar origin, to flow around the obstacle of Earth's magnetosphere [*Kivelson and Russell*, 1995]. The transition from the undisturbed solar wind to the magnetosheath slows the solar wind plasma, compresses it, and heats it. As the magnetosheath plasma flows around the magnetosphere, it is reaccelerated, expanded, and cooled – though not back to its original values, due to energy lost by the transition. The magnetosphere, in turn, is compressed on the sunward side and extended on the antisunward side, forming a comet-like or tear-drop-like shape. The antisunward portion of the magnetosphere is commonly referred to as the magnetotail.

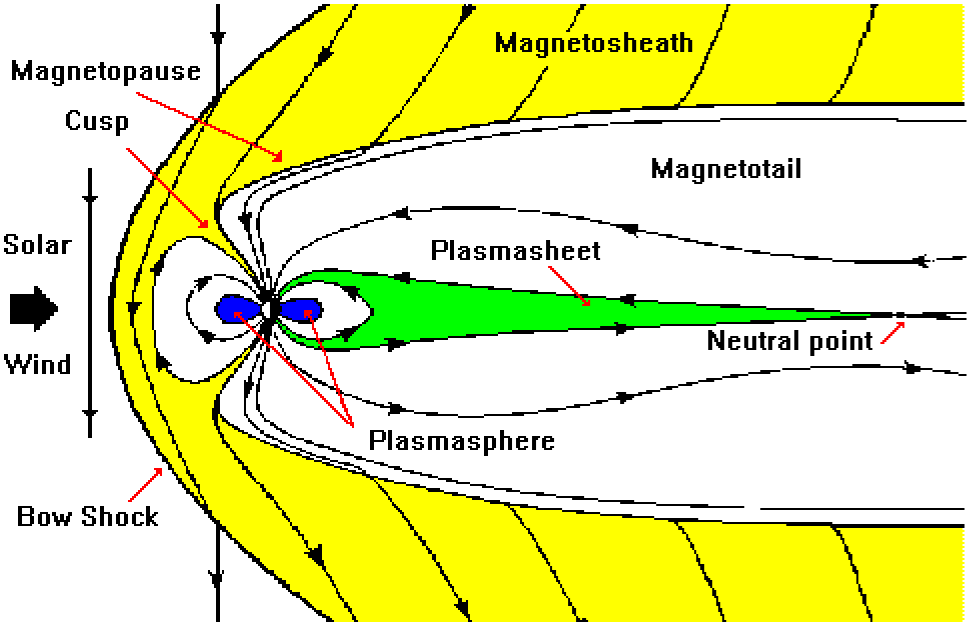

Figure 1-3. Meridional cut of the Earth, magnetosphere, and solar wind. [Image source: NASA.]

The boundary between the magnetosphere and the magnetosheath is the magnetopause, a “surface” (actually a thin region) on which the necessary currents flow to match the magnetic shear across the boundary, and across which the plasma velocity and density parameters begin to transition from magnetosheath conditions to magnetospheric conditions. In the sunward direction, the magnetopause location is determined by the balance of pressure between the magnetosheath momentum, which is typically much larger than the solar wind magnetic pressure, and the magnetospheric magnetic pressure, which is typically much larger than the magnetospheric plasma pressure. Under nominal solar wind conditions, the bowshock is located at about 15 R_E, while the sunward magnetopause is located at about 10 R_E.

Laterally, the magnetosheath plasma velocity becomes more aligned with the Sun-Earth line, and so exerts less dynamic pressure on the magnetopause; as a result, the total pressure inside the magnetosphere pushes the magnetopause out to the point where the two are in balance. Directly in the dawn and dusk directions, the magnetopause is typically located at about 16 R_E [*Sibeck et al.*, 1991], and continues to flare outward for several tens of R_E in the antisunward direction. The distance to the antisunward magnetopause is highly variable, since both the solar wind and magnetospheric pressures are very low in that region, and thus fluctuations in one can easily overbalance the other, but the distance is typically several hundreds of R_E and can reach 1000 R_E or more.

1.2.2 Brief anatomy of the magnetosphere

The Earth's magnetosphere is a highly complicated system, with a large number of current systems and regions of plasma populations, some of which can overlap and pass through each other. An idealized section of the magnetosphere is shown in Figure 1-4. Most of the currents and plasma populations are not relevant to this study, and so will not be discussed here, with the exception of the low-latitude boundary layer (LLBL), which forms through interaction between the magnetosphere and the solar wind (in the magnetosheath). This system will be discussed in more detail in a later section of this introduction.

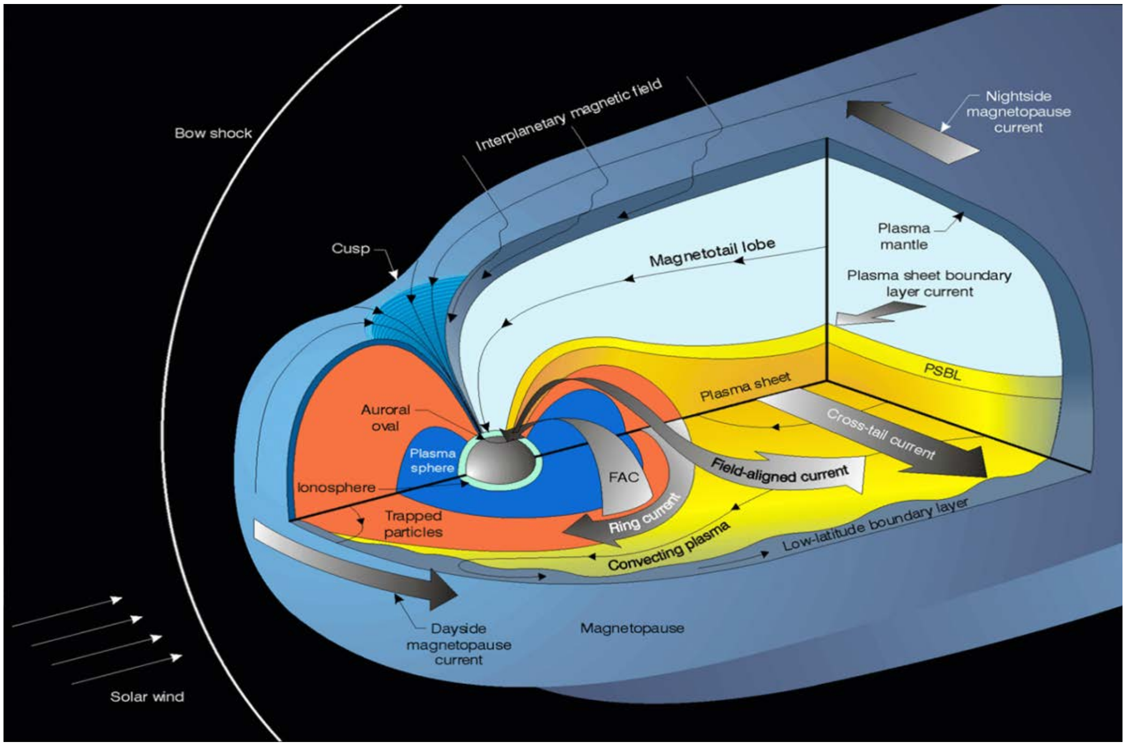

Figure 1-4. Anatomy of the magnetosphere. [Figure modified from figure in *Lopez*, 1990.]

1.3 Modes of interaction between the solar wind and magnetosphere

There are two main modes by which the solar wind transfers mass, energy, and momentum to the magnetosphere. The first, reconnection, is dependent on magnetic fields, whereas the other, the viscous interaction, is more of a mechanical interaction.

1.3.1 Reconnection

Magnetic reconnection was first proposed as a driver for ionospheric current observations by *Dungey* [1961]. In this model, if two magnetic field lines which are oriented in opposite directions are pushed together, field lines from each field can be broken and then "reconnected" to the other field, thus allowing plasma trapped on one field line to move to another field line (Figure 1-5). This process also energizes plasma in the reconnection region.

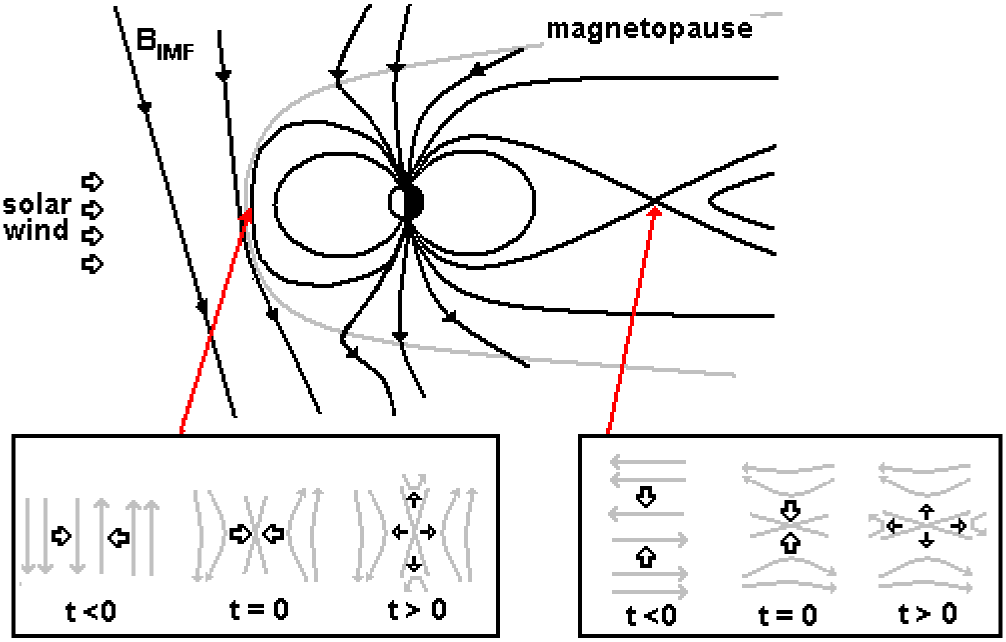

Figure 1-5. Reconnection on the sunward magnetopause and in the magnetotail.

Reconnection on the sunward magnetopause is strongest when the IMF is directed southward, opposite the direction of Earth's magnetic field in the equatorial region. In this case, a reconnection line will form near the intersection of Earth's magnetic equatorial plane and the magnetopause. At that line, "closed" magnetic field lines, which leave Earth's south geographic pole (a north magnetic pole) and run directly to the north geographic pole (a south magnetic pole), are broken and reconnect with solar wind magnetic field lines in the magnetosheath. These "open" field lines, which run from one terrestrial magnetic pole out into the solar wind, are pulled over the polar cap by the flow of the solar wind past the Earth. The open field lines collect in the magnetotail, where the magnetic pressure of the accumulation of field lines pushes open field lines in the center of the tail together, where they again undergo reconnection, turning two open field lines back into a closed terrestrial field line and a free solar wind field line. The terrestrial field line convects sunward, around the Earth, and back to the magnetopause, to continue the cycle. The newly-restored solar wind field line is pulled down the magnetotail and back out into the solar wind.

For northward IMF, the process is more complicated, with reconnection occurring at high latitudes, nearer the magnetic poles, but the reconnection process itself is the same. The cycle transfers much less energy to the magnetosphere for northward IMF, with otherwise similar solar wind parameters, than for southward IMF. An east-west IMF produces a more complicated process than southward IMF, with less energy transfer, but more than for northward IMF.

Reconnection can produce very complicated phenomena in the magnetosphere, such as magnetic storms, substorms, auroral displays, etc., but since those are not pertinent to the study at hand, they will not be discussed here.

1.3.2 Viscous interaction

1.3.2.1 Origin

The viscous interaction was first proposed by *Axford and Hines* [1961] as one possible driver for magnetospheric plasma circulation, which they proposed as the cause of ionospheric circulation (with Dungey's reconnection cycle proposed in that same paper as another possible driver). In the original idea, solar wind plasma flowing around the magnetosphere could interact with magnetospheric plasma on closed magnetic field lines, transferring energy and momentum, causing the magnetospheric plasma to move antisunward just inside the magnetopause, then circulate in toward the center of the tail, back toward and around the Earth to the sunward magnetopause, completing the cycle of plasma flow in a "viscous cell" (Figure 1-6). Observations have since confirmed the existence of a layer of anti-sunward flowing plasma just inside the magnetopause, though the plasma has some characteristics of magnetosheath plasma, raising unresolved questions as to its origins [*Eastman et al.*, 1976; *Sundberg et al.*, 2008, and references therein].

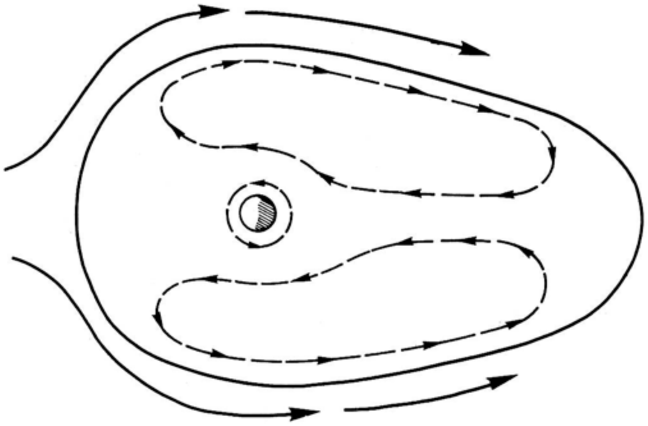

Figure 1-6. Viscous interaction with a closed magnetosphere. [From *Stern*, 1996.]

1.3.2.2 Mechanism

While *Axford and Hines* [1961] set up the idea of a viscous interaction between solar wind and magnetospheric plasma, no actual mechanism was proposed for the interaction. In a collisionless plasma (which describes most plasma between the Sun and Earth's ionosphere), the transfer of energy and momentum through such an interaction is not guaranteed ab initio. One leading theory for a physical mechanism is through the Kelvin-Helmholtz instability (KHI), which occurs when there is a velocity shear at the interface between two plasma populations [e.g., *Hasegawa*, 1975], producing rolled up layers of the two plasmas, known as Kelvin-Helmholtz vortices (KHVs). Evidence of KHVs has been observed in both *in situ* data and simulation results [*Claudepierre et al.*, 2008, and references therein].

1.4 The polar ionosphere, plasma convection, and the cross polar cap potential

The "frozen-in flux" condition of plasma and magnetic fields in the magnetosphere implies that the motion of plasma requires motion in the magnetic field, as well. Indeed, the motion of reconnected open field lines over the polar cap (Figure 1-7, for southward B_z) and then newly-closed field lines back to the sunward magnetopause can be traced along field lines to the ionosphere and observed in the motion of ionospheric plasma on those field lines, as can the circulation of plasma in viscous cells. Figure 1-8 shows the motion of ionospheric plasma circulation for an idealized case with southward B_z. (This motion is often called "convection," even though it is now known that it is not driven by temperature.) In the fixed frame of reference of the non-rotating Earth, plasma moving in a magnetic field must have an associated electric field [*Vasyliunas*, 2001], given by $\mathbf{E}=-\mathbf{v}\times\mathbf{B}$. Since the terrestrial magnetic field is approximately radial at high-latitudes, the convective electric field points approximately horizontally, perpendicular to the plasma flow at all points.

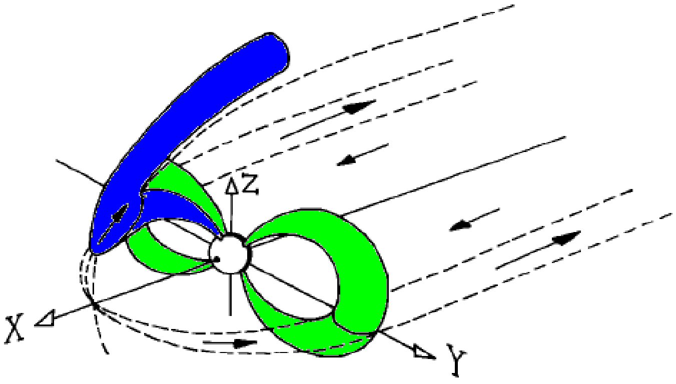

Figure 1-7. Magnetic field and plasma flow due to reconnection (blue) and viscous interaction (green). [Modification of figure from *Cowley*, 1982.]

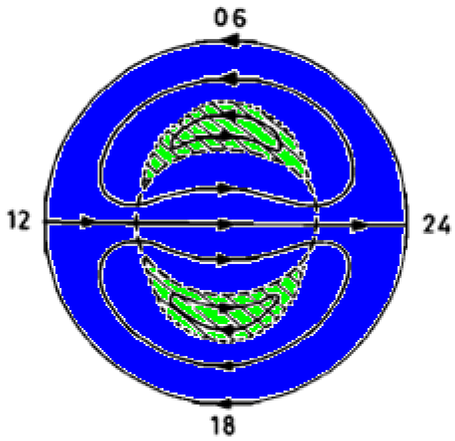

Figure 1-8. Ionospheric plasma flow due to reconnection (blue) and viscous interaction (green). [Modification of figure from *Cowley,* 1982.]

The electric field E can be expressed as the negative gradient of the electrostatic potential, **E**=-∇Φ, and conversely the electrical potential between any two points can be found by integrating along the path thus: Φ=∫(**E**·**dl**). Thus, with the electric field defined at all points over the polar ionosphere, a potential map can also be constructed. Since potentials are only defined to within an additive constant (**E**=-∇Φ=-∇(Φ+C)), a reference point must be chosen in order for the potential map to assume unique values. In the polar ionosphere, a low-latitude point where convective electric fields are close to zero (~50°), is often chosen as Φ=0, with all other points defined with reference to that point [*Hairston et al.*, 1998; *Merkin and Lyon*, 2010].

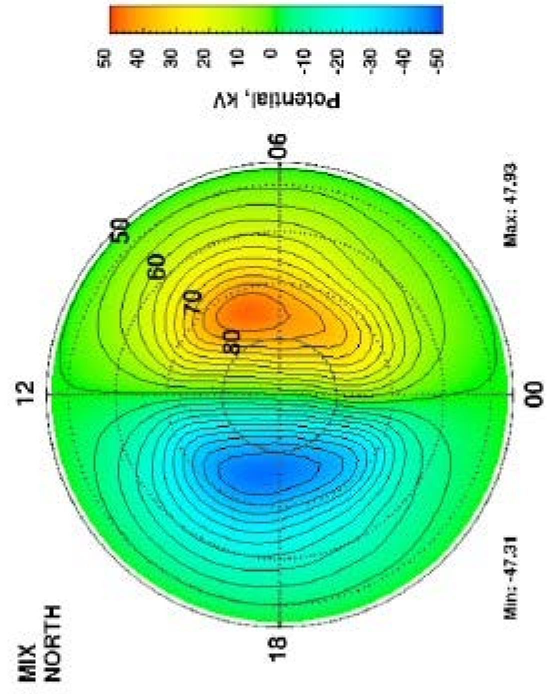

Figure 1-9. Sample ionosphere from the LFM-MIX simulation. The image has been rotated to match the orientation of Figure 1-8. [From *Merkin and Lyon*, 2010.]

Figure 1-9 shows an ionospheric potential pattern from the LFM simulation, for fairly standard conditions (solar wind n = 5 cm^{-3}, V_x = -500 km s^{-1}, B_z = -5 nT). The potential difference between the two extrema defines the cross-polar cap potential (CPCP or Φ_{PC}): $\Phi_{PC} = \Phi_{max} - \Phi_{min}$. Φ_{PC} is often used as a proxy for magnetospheric convection. Note that the potential extrema occur in the regions defined in Figure 1-8 as mapping to the viscous cells, but that much of the potential difference occurs in the region mapping to reconnection-driven flow. Thus, for southward B_z, Φ_{PC} is a combination of contributions from both the viscous interaction (the "viscous potential" or Φ_V) and reconnection (the "reconnection potential" or "merging potential" or Φ_R).

While southward B_z produces two cells of circulating plasma in the ionosphere, northward B_z produces four cells – two reconnection-driven cells near the magnetic pole and two viscous-driven cells at lower latitudes. The potential extrema in this case are usually on either the two viscous cells or on the two reconnection cells, with the potential due to the other two cells being "eclipsed" by the two dominant cells, and so making no contribution to Φ_{PC} [*Bhattarai et al.*, 2012 and references therein].

1.5 Previous studies involving the viscous interaction

The cross-polar cap potential can be measured using a variety of methods, including low-altitude satellite passes through the ionosphere (such as the DMSP satellites [e.g., *Hairston et al.*, 1998]), ground-based radar signals backscattered from ionospheric plasma (such as the SuperDARN network, [e.g., *Shepherd and Ruohoniemi*, 2000]), and algorithms which assimilate electromagnetic data from a variety of sources (such as AMIE, the Assimilative Mapping of Ionospheric Electrodynamics [*Richmond and Kamide*, 1988; *Ridley and Kihn*, 2004]). Each method has relative advantages and disadvantages, but none of these techniques can separate the viscous and reconnection potentials from each other, as can be seen in Figure 1-9. There are several methods that have been useful in finding the viscous potential, though.

1.5.1 Observations, direct and indirect

1.5.1.1 Extrapolation of CPCP to zero B_z

The first technique which yielded a value for the viscous potential was to collect a number of Φ_{PC} values measured by satellite passes through the ionosphere and plot them against the solar wind B_z value or some function of it, then extrapolate to $B_z = 0$ nT, at which point there should be no reconnection of the north-south components. *Reiff et al.* [1981] were the first to use this technique, using only southward B_z observations. They found that out of a dataset with potentials ranging from about 30-140 kV, merging could not account for about 35 ± 10 kV. *Doyle and Burke* [1983] used a similar technique with a different dataset and also found a residual potential of about 40 kV which could not be accounted for by merging, though they pointed out that if the analysis by *Wygant et al.* [1983] is correct, the ionosphere needs time to "spin down" after high levels of activity, and so the non-merging component could be as low as 20 kV. *Boyle et al.* [1997] took this into account by looking only at periods with quasi-steady solar wind conditions, which yielded a dataset with potentials in the range of about 5-170 kV. They also fitted the non-merging component data, and found that it was best accounted for by a term equal to $10^{-4} V^2$, where V is the magnitude of the solar wind velocity. For comparison, a solar wind speed of 400 km s^{-1} yields a non-merging potential of 16 kV with this formula, and a solar wind speed of 600 km s^{-1} yields a non-merging potential of 36 kV. *Burke et al.* [1999] looked at datasets from two satellites and found non-merging residuals of 32.6 kV and 34.4 kV, but those data were not restricted to steady solar wind conditions, and so could be influenced by other sources, such as the neutral flywheel effect. *Shepherd et al.* [2003] fit SuperDARN data to the Hill model [*Siscoe et al.*, 2002] and found a residual value of 17 kV that could not be explained by reconnection (though it is worth noting that potentials measured by SuperDARN tend to be lower than those measured by satellites for the same conditions, so that residual potential would also presumably be lower than a satellite would measure by the same factor (see discussion in *Wilder et al.* [2011])).

1.5.1.2 Satellite passes through the LLBL

Another method of measuring the viscous potential is by using data from satellite passes through the LLBL. *Mozer* [1984] used satellite passes through the LLBL near the local dusk sector to measure the electric field in that region, and thus calculate the potential across the LLBL (which should be mapped to the ionosphere, producing a viscous cell and the same potential there). They found that the LLBL was thinner than expected and had weaker electric fields than expected, resulting in an average total potential from the LLBL on both flanks of about 5 kV, which is less than 10% of what they consider to be the typical CPCP of 60 kV (though values did reach as high as 16 kV). *Heikkila* [1986] disputed the analysis, providing an alternate analysis that came up with a boundary layer potential around 30 kV, though *Mozer* [1986] did not agree with that reinterpretation, but also pointed out that there is considerable difficulty in studies of this type, due to frequent rapid motion of the LLBL as a satellite traverses it, plus difficulties in finding the actual edges of the LLBL from data. *Hapgood and Lockwood* [1993] examined some of those difficulties, and also found very low potentials in a single satellite pass through the dawnside – around 3 kV. Similar results were also obtained in *Mozer et al.* [1994].

1.5.1.3 Mapping the LLBL to the ionosphere

One more method of measuring the viscous potential is by looking at the properties of plasma on field lines in the ionosphere, in an attempt to determine which regions map to the viscous cells. *Newell et al.* [1991] set out a system for identifying the LLBL based on particle data in the ionosphere, finding a related potential that averaged around 5 kV, though the largest of the 9 cases analyzed reached 15 kV. *Sundberg et al.* [2008] performed a similar type of analysis for a large number of cases with negative B_z and ran statistical analyses on the results. They found an average low-latitude potential of only 1-2 kV, though the results of that paper raise some questions, since their high-latitude (reconnection-driven) potentials do not extrapolate to near zero at zero B_z, as expected, but rather extrapolate to around 40 kV, which is similar to the *Reiff et al.* [1981] analysis and results. *Sundberg et al.* [2009] examined northward B_z, and found a larger potential associated with the boundary layer – averaging around 9.8 kV, with a solar wind dependence that best matched $n^{1/2}V^2$. This is significant in that it matches the form of the viscous scaling factor found by *Newell et al.* [2008], which will be discussed later in this dissertation (though it is not clear that the higher viscous potential for northward B_z is compatible with very recent results by *Bhattarai et al.* [2012] which find that the viscous potential is constant for southward B_z but decreases for northward B_z). *Drake et al.* [2009] made a detailed comparison of the dawn and dusk LLBLs for southward B_z, finding an average total potential of 7.6 kV, but they also noted that for some conditions, the potential from the LLBL can be up to 30%, with an implication that the peak in the potential might not be along the dawn-dusk line.

Blomberg et al. [2004] provided some possible clues as to the discrepancy between the different ranges of potentials ascribed to the viscous interaction by different study methods. They studied magnetospherically active times, using a different dataset (6 passes of the Freja satellite), and found that the LLBL contributed, on average, at least ⅓ of the CPCP (around 20 kV) and possibly as much as ½ of the CPCP (around 30 kV), with high values possibly up to 48 kV (out of 83 kV total). They suggest that one possible reason that these values are so much higher than *Mozer* [1984] (and by implication, some other studies) is that the center of the viscous cells might be farther down the tail than the dawn-dusk line, where the passes that *Mozer* [1984] analyzed were located. Unfortunately, *Blomberg et al.* [2004] has received little attention, so this possibility has not been explored up to this point in time.

1.5.2 Simulation results

There are very few simulation studies of the viscous interaction. *Sonnerup et al.* [2001] ran the ISM MHD code with near-zero IMF, for a number of solar wind velocity values and ionospheric Pedersen conductance (Σ_P) values. Their results found a velocity dependence given by $\Phi_{PC} = 3.5(V_{SW} - 185)^{0.4}$ at $\Sigma_P = 6$ mhos. For $V_{SW} = -400$ km s^{-1}, this gives the value 29.9 kV. The conductance dependence is slightly more complicated: $\Phi_{PC} = 109.6/(8.1 + \Sigma_P)^{1/2}$ at $V_{SW} = -400$ km s^{-1}. *Watanabe et al.* [2010] also looked at the viscous interaction in simulations, using the BATS-R-US MHD code, with runs using solar wind conditions of V_{SW}=-400 km s^{-1}, n=5 cm^{-3}, B_x=0 nT, B_y=4 nT, B_z=2 nT, ionospheric Σ_P=1 mho, and 3 different dipole tilt angles. The purpose of the study was to look at ionospheric and magnetospheric morphology, not the viscous potential itself, but the simulation results did show clear viscous cells, and for zero dipole tilt (which is often the value used in simulations), Φ_V=~10 kV, which was ~20% of the total Φ_{PC}=~50 kV. Since Σ_P was very low (MHD simulations are often run with a value of Σ_P in the range of 5-10 mhos), the potentials in the simulation are probably higher than would be observed in reality, but the relative ratios would likely be the same. Φ_V showed a linear response to dipole tilt angle over most of the range tested (-35°, -20°, 0°, +20°, and +35°), with a maximum of ~15 kV at -20° and a minimum of ~3 kV at +35°. It is worth noting that the simulation was run with northward B_z, which is now known to reduce the viscous interaction (see Chapter 0 4.2); it is unknown at this point if B_y affects the viscous interaction, but indications from *Mitchell et al.* [2010] imply it does not. Thus, it is not clear how comparable these viscous potential values are to values obtained from southward B_z conditions. There are many other publications based on MHD simulations of the magnetosphere, but they generally do not examine the viscous potential.

1.6 Motivation for this research

In nature, conditions which would produce a purely viscous cross-polar cap potential seldom occur, and even a viscous-dominant CPCP is seldom steady and persistent enough to get an unambiguous measurement, much less to find a functional dependence on solar wind parameters. Since the viscous and reconnection potentials are generally mixed for southward B_z, uncertainty in the value of the viscous potential means increased uncertainty in the reconnection potential and the energy transfer that it represents. Computer simulations, on the other hand, allow us to input arbitrary conditions and get results with whatever temporal and spatial resolution the simulation runs at. We can also run the simulation for a planned range of parameters to systematically study the dependence of the viscous interaction to a variety of solar wind and ionospheric parameters.

1.7 Preview of the rest of this document

The rest of this dissertation is organized as follows. Chapter 2 looks at the Lyon-Fedder-Mobarry (LFM) MHD simulation, as well as several techniques for finding the viscous potential using LFM. Chapter 3 systematically analyzes the effect of several solar wind and ionospheric parameters on the viscous potential in LFM, culminating with a semi-empirical formula for the viscous potential in LFM. Chapter 4 compares that formula first to an empirical scaling relation for the viscous potential, then compares the viscous potential formula to an LFM run with real solar wind input and finds a scaling factor to bring the LFM results down to more realistic values. Chapter 4 also uses LFM results to turn the empirical scaling factor into an independent formula for the viscous potential and compares it to the viscous potential formula and the scaled-down LFM run, and finally compares the scaled-down LFM potentials to the results of an independent empirical CPCP model. Chapter 5 summarizes this work and discusses possible directions for future research.

CHAPTER 2

FINDING THE VISCOUS POTENTIAL IN THE LFM SIMULATION

2.1 Overview of the LFM MHD simulation

2.1.1 Magnetohydrodynamics (MHD)

Magnetohydrodynamics (MHD) is a branch of plasma physics in which the plasma is treated as an electrically charged and conducting fluid, which thus reacts to magnetic fields, as well. This allows for treatment of much larger quantities of plasma to be simulated (such as the magnetosphere) than could be handled if every particle's motion had to be calculated, but at the expense of effects that are based on individual particles. The equations are modifications of standard hydrodynamics, with Maxwell's equations and Ohm's law included [*Kallenrode*, 2004]. These equations are prohibitively impractical to solve analytically except for some very simple cases. Fortunately, the advancement of computer technology has made it not only possible to perform simulations based on the MHD equations [e.g., *Lyon et al.*, 2004; *Powell et al.*, 1999; *Raeder et al.*, 2008; *Palmroth et al.*, 2005], but in the past decade that technology has become readily and inexpensively available.

2.1.2 A Global, 3-D simulation; the LFM grid

The model we have used in this study is the Lyon-Fedder-Mobarry (LFM) global 3-D MHD simulation. It has been in development since the mid-1980s [*Lyon et al.*, 2004], with constant refinements and improvements being added regularly. LFM is based on a distorted spherical grid, with its axis of symmetry aligned with the GSM x-axis (Figure 2-1). The rest of the grid is modified to concentrate grid points in regions where higher levels of detail are known, a priori, to be needed – such as the sunward magnetopause and magnetosheath - at the expense of regions that are known to be less significant for the simulation development – such as the distant magnetotail (Figure 2-2).

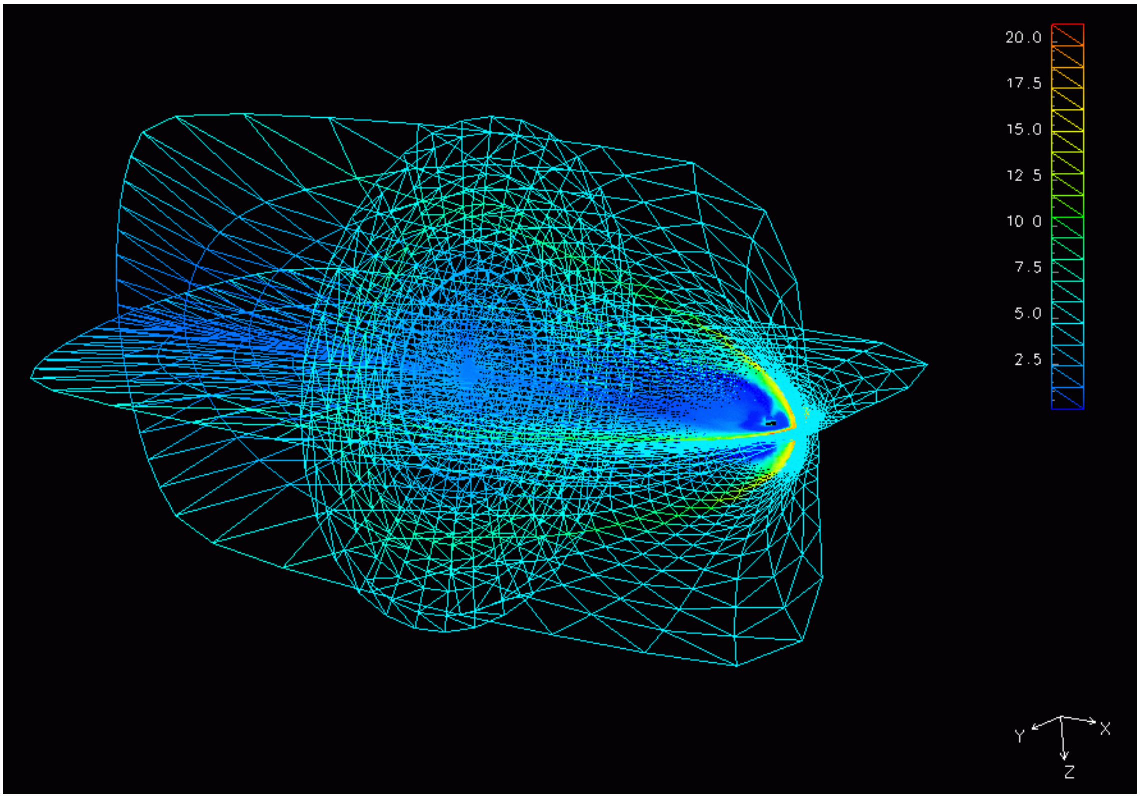

Figure 2-1. The LFM grid, with density mapped to lines connecting grid points.

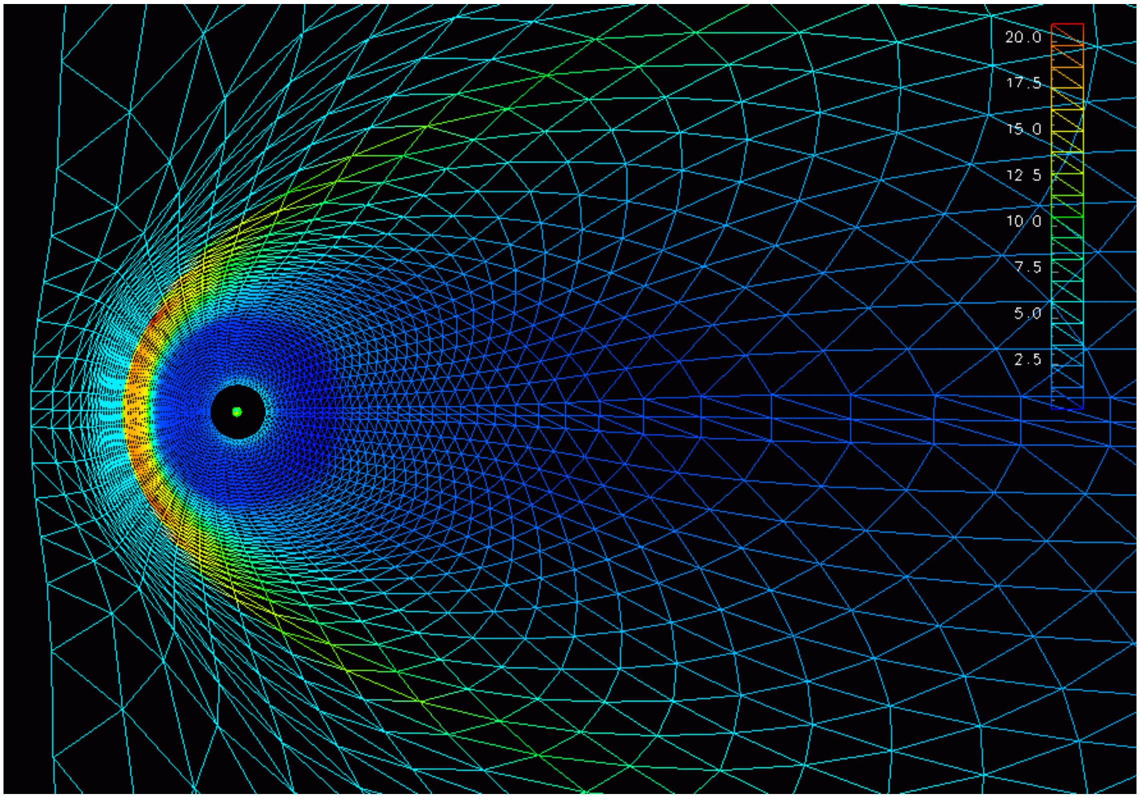

Figure 2-2. Closer view of the equatorial plane of the distorted grid, showing the increased resolution at the sunward magnetopause and magnetosheath.

Grid resolution and dimensions can be changed, but the LFM grid typically extends about 25 R_E sunward from the center of the Earth, 100 R_E laterally, and about 300 R_E antisunward. The timestep in LFM is partially determined by the speed of the fastest wave in the simulation, so a spherical boundary is removed from the center of the grid, inside of which higher wave speeds would make timesteps too short to find solutions in a reasonable amount of time. For the simulations analyzed here, that boundary is 2.8 R_E. The grid itself extends 50 points radially, 32 points azimuthally, and 24 points latitudinally, for 38,400 points in the "single resolution" grid. Higher resolution grids can be used, with the highest resolution grid currently containing 8 times as many grid points in each direction as this version, but each doubling of grid resolution incurs at least a 16-fold increase in computation time – 2-fold for each spatial dimension, plus a 2-fold increase for the necessary reduction in the timestep. Current desktop/server computer technology, using 8 computer cores, allows the single-resolution version to run approximately 3 times faster than real time (1 hour on the computer produces 3 hours of simulation time). Since most codes and computer architectures do not scale linearly as the number of cores increases, it is not surprising that the 8x resolution code is only run on multi-thousand core supercomputers. (We would point out that a 4-processor computer that our lab purchased 7 years ago for $16k could only run this code at ½ real time. The current computer cost 1/10 as much (2 years ago) and runs 6x faster, so the limitations described here will probably seem antiquated within 10 years.)

2.1.3 Boundary conditions and the ionospheric simulation

The LFM grid has two boundary surfaces: an external, roughly cylindrical surface composed of the points on the outer surface of the distorted spherical grid, and an internal sphere, closest to the Earth. The external boundary receives its inflow conditions on the sunward surface and the sides from the solar wind file, which can come from a variety sources, so long as it provides the required data. Common sources include idealized solar wind conditions (which were used to produce the results in Chapter 3 of this dissertation), real solar wind data from satellite measurements (such as from ACE or WIND) or modifications thereof (which were used to produce the results in Chapter 4), and the output of solar wind computer models. The latter – chaining a set of computer models together, with the output of one feeding the input of another, from the Sun to the Earth – has been the mission of the Center for Integrated Space Weather Modeling (CISM) [*Hughes and Hudson*, 2004]. While the solar wind bounds the front and sides of the LFM grid, the tail – the antisunward "cap" of the cylinder – provides supersonic and super-Alfvénic outflow only, so plasma can exit through that surface, but no inflow is allowed.

The internal boundary in LFM maps directly along magnetic field lines to a 2-D ionospheric simulation. Field aligned currents (Birkeland currents) reaching the inner boundary of LFM are mapped to the ionospheric simulation and provide the source term ($j_{||}$) in the equation

$$\nabla \cdot \Sigma \cdot \nabla \Phi = j_{||} \sin \delta$$

Equation 1

where Σ is the conductivity tensor, Φ is the electrostatic potential, and δ is the magnetic inclination or dip angle (the angle between the magnetic field direction and a horizontal line).

In a resistive plasma, such as the ionosphere, conductivity takes finite values, which generally differ in the directions parallel to or perpendicular to the ambient magnetic field. An external electric field further breaks the symmetry. Conductivity and currents that are perpendicular to the magnetic field but parallel to the electric field are called Pedersen conductivity and currents (Figure 2-3). Hall conductivity and currents are perpendicular to both the magnetic and electric fields. Birkeland (or field-aligned) conductivity and currents are parallel to the magnetic field. Typically, field aligned conductivity in the ionosphere is several orders of magnitude larger than either Hall or Pedersen conductivity, which can vary in relation to each other depending on height. Hall currents generally form closed loops within the ionosphere, whereas Birkeland currents flow into the ionosphere, turn into Pedersen currents as they flow through the ionosphere (due to the existence of the ionospheric convective electric field), and then flow back out as Birkeland currents again.

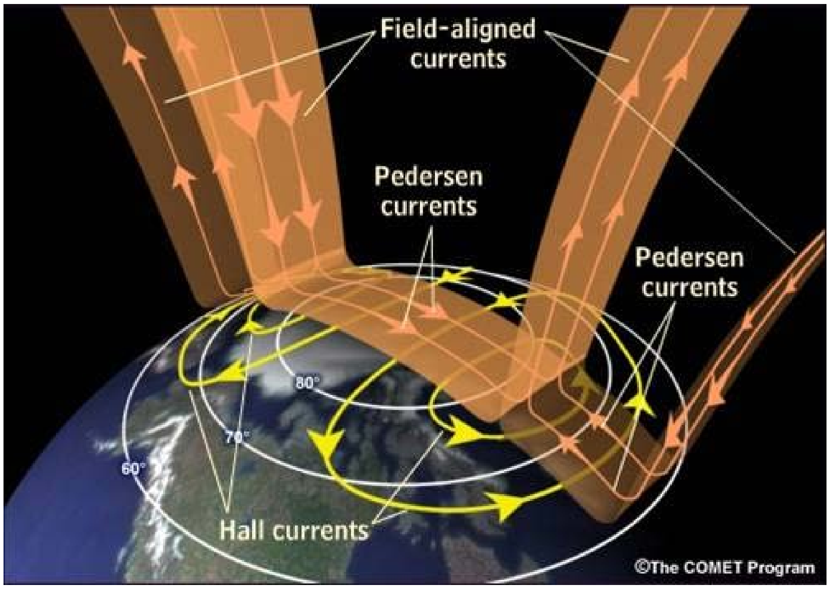

Figure 2-3. Typical ionospheric currents: Hall, Pedersen, and Birkeland (field-aligned).
[Source: The Comet Program.]

In LFM, ionospheric conductivity can either be set to a constant value or be determined by an empirical model. For constant conductivity, the input value is the Pedersen conductivity, which is constant and uniform over the entire ionosphere. Alternately, the Hall and Pedersen conductivity can be defined for each point on the ionosphere by an empirical model, which uses solar F10.7 flux as input and allows modifications to the conductivity from particle precipitation [*Fedder et al.*, 1995; *Wiltberger et al.*, 2009].

The procedure LFM follows is that the MHD simulation completes the calculations for one timestep, which determines the Birkeland currents impinging on the inner boundary. Those currents are mapped down to the ionospheric grid at 1 R_E along magnetic field lines, and the ionospheric calculation above is solved for Φ at each point on the grid. Those values are then mapped back out to the LFM inner boundary along field lines, and the next LFM timestep uses the new potentials in its calculations.

Unless otherwise stated, all LFM runs described here have been run with a uniform Pedersen conductance of 10 mhos (1 mho = 1 S = 1 siemen). This value was found to give more realistic results than the more common value of 5 mhos [*Lopez et al.*, 2010] and to provide the most realistic magnetopause shape [unpublished work by Kevin Pham, by comparing to results in *Sibeck et al.*, 1991].

2.2 Evidence of the viscous interaction in LFM

Ideal MHD does not, in fact, have a viscosity term, as normal hydrodynamics does. This raises the question of whether an MHD code can be used to study the viscous interaction. There are several reasons why we are convinced it can.

First, MHD codes were initially expected to fail to produce any reconnection-driven processes, since ideal MHD does not produce magnetic reconnection. And yet numerical effects inherent in the encoding of the MHD equations for calculation by computers produces a reconnection-like process that has, at least so far, proven to yield results that are remarkably similar to real reconnection [e.g., *Goodrich et al.*, 1998; *Wiltberger et al.*, 2000]. This does not mean that a viscous interaction can be guaranteed to appear in the LFM output, but it certainly means that such a possibility cannot be dismissed a priori.

Secondly, the lack of an explicit viscosity term does not preclude a viscous interaction. Since the exact mechanism behind the viscous interaction is unknown, it is not clear whether that mechanism is, in fact, modeled by the MHD code. If the mechanism is the Kelvin-Helmholtz instability, then it is entirely possible that LFM and other MHD codes are capturing the viscous process, as KH vortices have been seen in LFM [*Claudepierre et al.*, 2008; also see Figure 2-4].

Furthermore, physical processes expected to result from a viscous interaction can very clearly be seen in the output of the LFM code. Figure 2-4 shows two cut planes with velocity mapped to them, from an LFM run with fairly typical solar wind and ionospheric conditions. These show anti-sunward plasma flow inside the magnetopause, which is a predicted result of a viscous-like interaction. That figure also shows a velocity field, in which arrows show direction of plasma velocity but not magnitude; structures that may be Kelvin-Helmholtz vortices are clearly visible. The shape of one such vortical structure is traced by a red velocity streamline, which is shown to be inside the magnetosphere by the closed magnetic field line, in green. Note that the streamline shows the path a particle would take if the velocity field were static; a real particle would likely take a different path, as the velocity field evolved in time.

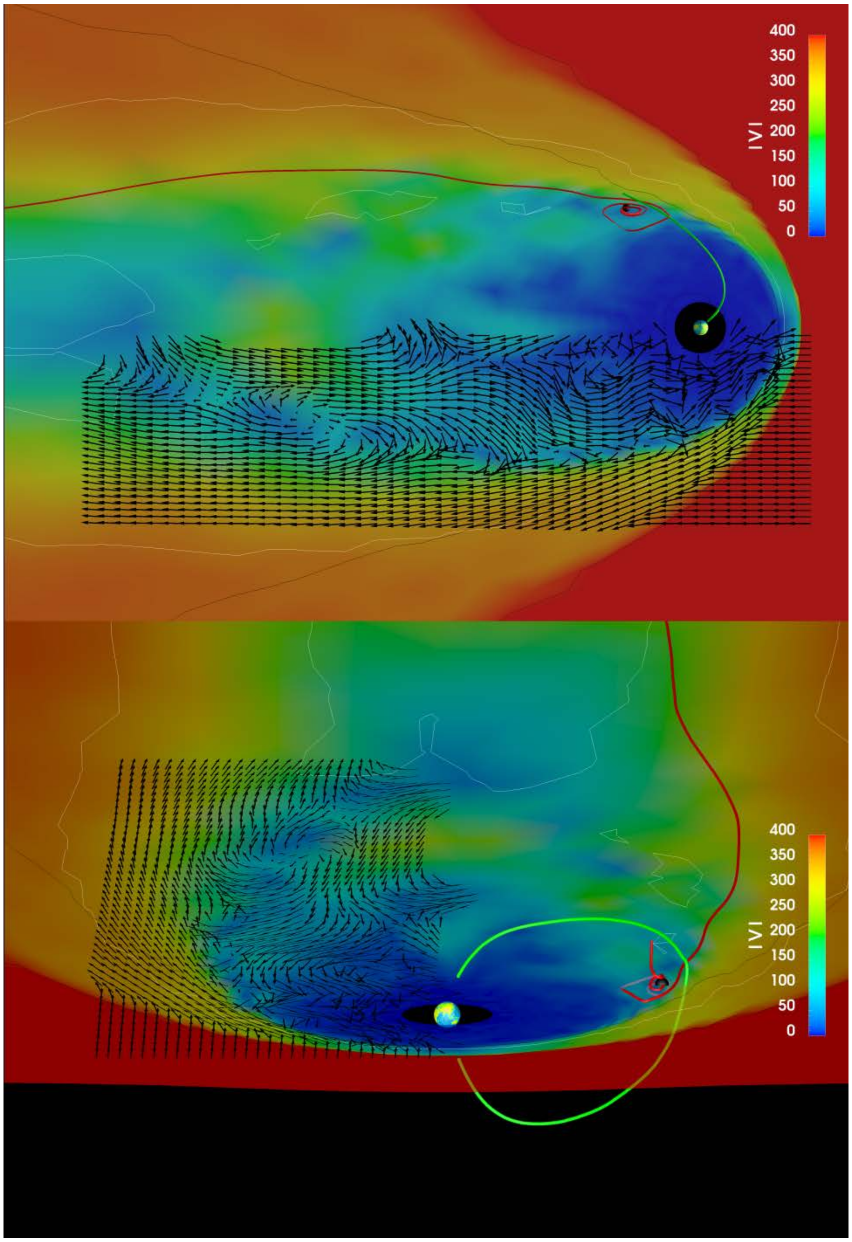

Figure 2-4. Velocity cut planes from an LFM run. The vector field shows direction but not magnitude. Vortical structures are visible along the magnetopause. The vertical structure traced by the red velocity streamline is shown to be inside a closed magnetic field line (green), and thus inside the magnetosphere. [From *Bruntz et al.*, 2012a]

One final piece of evidence for the a viscous interaction in the LFM code is that the cross-polar cap potential does not drop to zero as the IMF goes to zero, as would be expected if magnetic reconnection were the only driver of magnetospheric convection. This result will be explored further in the next section.

2.3 Methods of finding the viscous potential in LFM

We have used several methods of finding the viscous potential in the LFM simulation. Each will be discussed in turn here, then they will be compared, and we will explain why we chose the method used in Chapter 3.

2.3.1 Extrapolating the CPCP to zero Bz

Following the general idea of *Reiff et al.* [1981], we should be able to plot the CPCP for several small values of negative IMF B_z (small enough that the magnetosphere responds linearly, and stays out of the saturation regime – see, e.g., *Russell et al.* [2001]), which will include potentials from both reconnection and viscous interaction. We then extrapolate those points to zero B_z, at which point the reconnection contribution will also be zero. The CPCP corresponding to a given set of solar wind conditions is not a simple matter, though.

Figure 2-5 shows the time series of the CPCP ($\Phi_{PC} = \Phi_{max} - \Phi_{min}$, where the extrema are found over the entire polar ionosphere) for an LFM run with solar wind conditions $n = 5$ cm^{-3}, $V_x = -400$ km s^{-1}, and $B_z = -3$ nT. The simulation initializes the LFM grid from 00:00-00:50 ST (simulation time) with minimal solar wind input, to initialize the grid and allow the magnetosphere to take shape, then switches to $B_z = -5$ nT for 2 hours, which turns on reconnection, quickly raising the CPCP. At 02:50 ST the IMF switches to $B_z = +5$ nT for 6 hours, which quickly decreases reconnection and the CPCP. At 08:50 ST the IMF switches to the B_z value to be studied (in this example, -3 nT) and the CPCP soon settles on a steady-state value. The solar wind density and velocity are held constant throughout the run.

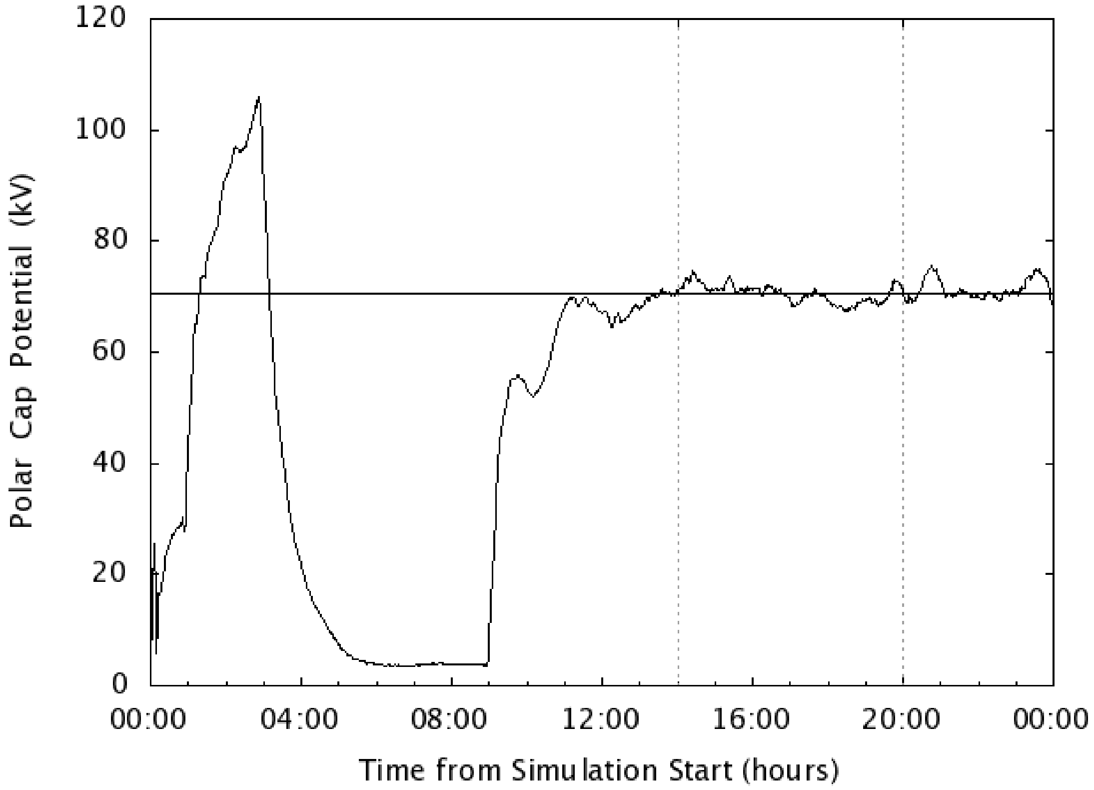

Figure 2-5. Polar cap potential for an LFM run, with the averaging period marked. [From *Bruntz et al.*, 2012a.]

As can be seen, the CPCP does not always settle down to a constant value after the initialization period. The "steady-state" value might in some cases be more properly called a "quasi-steady-state" value. As a result, the CPCP must be averaged over a time period, rather than simply picking one arbitrary point in time. Any averaging period should exclude the initialization period, as well as the initial response to the new solar wind values. We tried several averaging time periods, starting at 14:00, 16:00, and 18:00 ST, then averaging for 2, 4, or 6 hours, but not past 20:00 ST. We performed these averages over the output from several different LFM runs, which had different amounts of variability in the CPCP values.

In all runs tested, we found that the averages for these time periods tend to cluster in a very small range, and that the range of averages (largest minus smallest) was always less than 10% of the smallest average value (and thus an even smaller percentage of the other values). This shows that the average CPCP is not sensitive to the starting time or length of the averaging window, within this range. For comparison, the largest average CPCP for the run shown in Figure 2-5 was 71.96 kV, while the smallest was 69.90 kV – a difference of only 2.06 kV, which is only 2.9% of the smallest value. The fluctuations of the CPCP within those windows are actually relatively small as well – the standard deviations of the data in each window ran from a low of 0.9511 kV to a high of 1.5816 kV, compared to a mean around 70 kV. All datasets tested had similar results. We chose to average over the 6 hour window from 14:00 ST to 20:00 ST, in order to minimize the effects of any fluctuations.

Applying this technique to each LFM run, we get a single data point for every set of solar wind conditions (density, velocity, IMF B_z value). We can run four LFM runs with B_z = -1, -2, -3, and -4 nT and constant solar wind density and velocity, and from those four data points extrapolate back to B_z = 0 nT, to predict the expected viscous potential for those solar wind and ionospheric conditions (following the method used in *Lopez et al.*, [2010]) (Figure 2-6).

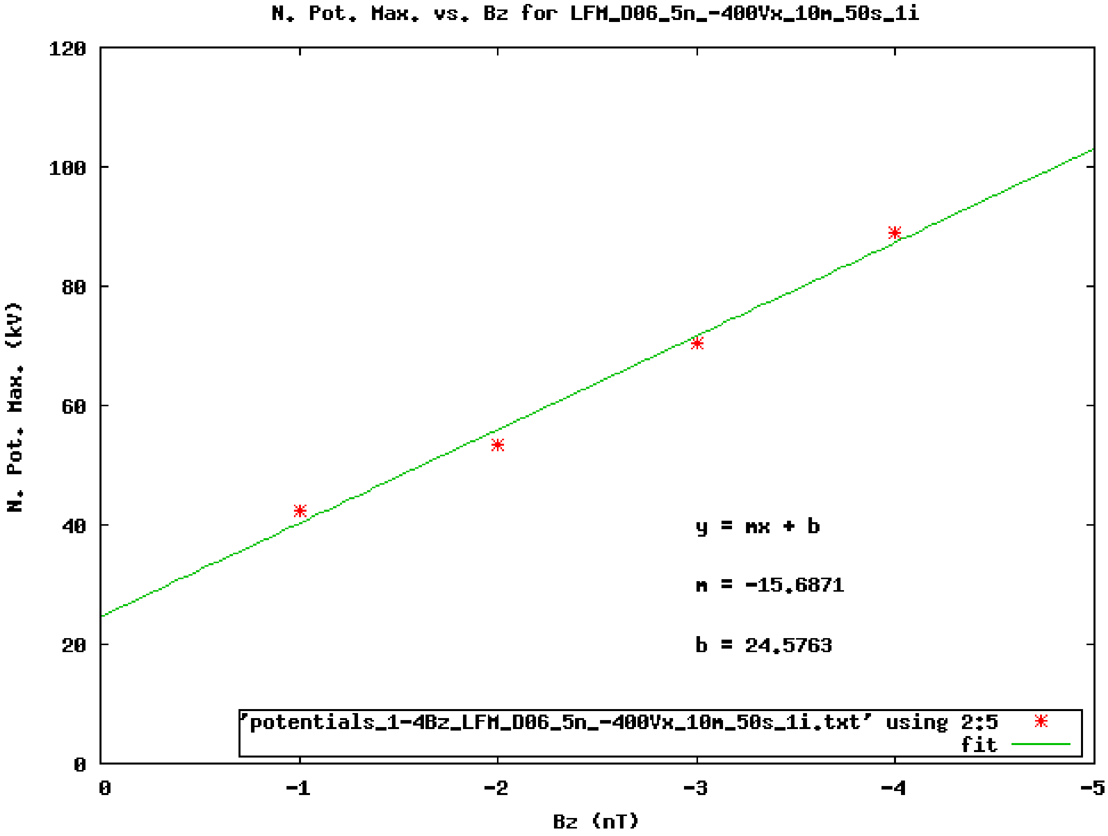

Figure 2-6. Extrapolation of -1 to -4 nT B_z data points to B_z = 0 nT. V_x = -400 km s^{-1}, n = 5 cm^{-3} for these runs.

2.3.2 Zero IMF method

Another method for finding the viscous potential in LFM is to simply run the simulation with zero IMF. In this case, there is no solar wind magnetic field to reconnect with the terrestrial magnetic field, so the entire CPCP is from the viscous interaction. This method has the advantage that it takes about ¼ the time of the extrapolation method (and less than that, if the extrapolation method includes the 0 nT point), since only one LFM run needs to be completed, rather than 4 (or 5). One disadvantage is that the extrapolation method will tend to reduce the effect of a single data point that takes a particularly high or low value when the fit is performed; the zero IMF method has no such method to mitigate the effects of wayward data points. Nevertheless, the standard deviation from the potential averaging step tends to be very small in LFM runs, as was mentioned previously, so this hazard is not considered to be large.

2.3.3 Streamline tracing method

One last method that we have used is to find the outer ends of the reconnection line on the magnetosphere and trace them sunward, back into the solar wind, and find the projection parallel to the interplanetary electric field (IEF), which is found from $\boldsymbol{E} = -\boldsymbol{V} \times \boldsymbol{B}$. For a solar wind velocity parallel to the x-axis and magnetic field parallel to the z-axis, $E = -V_x B_z$. The geoeffective length L_G times the IEF should give the potential that is applied across the reconnection line – the reconnection potential Φ_R (Figure 2-7). For southward B_z, the CPCP (Φ_{PC}) is the sum of reconnection and viscous potentials: $\Phi_{PC} = \Phi_R + \Phi_V$, so it follows that $\Phi_V = \Phi_{PC} - \Phi_R$. Having found Φ_R from tracing field lines and Φ_{PC} from the ionosphere, we now have Φ_V, as well.

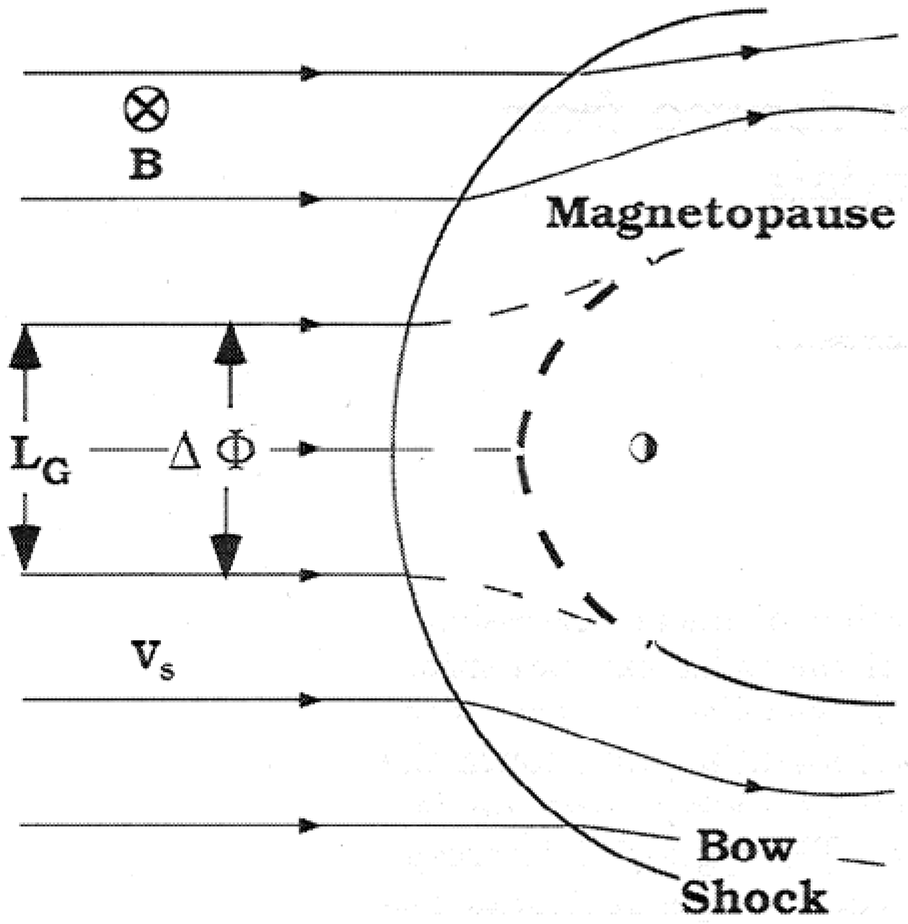

Figure 2-7. Geoeffective length (L_G) in the solar wind maps to the reconnection line on the magnetopause. [From *Burke et al.*, 1999]

This method was used by *Merkin et al.* [2005] to find a rough value for the extent of the reconnection line; *Lopez et al.* [2010] refined the technique to get more precise values of L_G.

There are a few disadvantages to the streamline tracing method of finding the viscous potential. One large disadvantage is that it is time-consuming, requiring careful consideration of the system being analyzed, and we have so far been unsuccessful in finding a method to automate the process. This also brings some subjectivity into the results, since two people analyzing the system might not come up with the exact same values for L_G. As seen in *Lopez et al.* [2010] and *Bruntz et al.* [2012a], however, it can provide reliable results.

2.4 Comparing results of each method

Table 2-1 shows a comparison of the viscous potential found through the three methods described here. Columns 1 through 3 tell the solar wind conditions for which the various viscous potential values are calculated. Column 7 shows the viscous potential calculated based on the streamline tracing (geoeffective length) method; column 8 comes from the zero IMF (0 B_z) method; and column 9 comes from the extrapolation to 0 B_z method. Note that columns 4-6 are used in the calculation of column 7 (streamline tracing). Also note that the zero IMF method (column 8) is based on B_z = 0 nT, not the B_z value in column 1; and the extrapolation method (column 9) is independent of IMF, so their values don't change in rows 1 and 2, nor do their values change in rows 3 and 4.

Table 2-1. Comparison of viscous potential found by various methods:
Streamline tracing (column 7), Zero IMF (column 8), and Extrapolation of B_z to 0 nT (column 9).

B_z (nT)	V_x (km/s)	n (#/cc)	L_G (R_E)	L_G*V_x*B_z *(6.371) (kV)	Φ_{PC} (kV)	$\Phi_V = \Phi_{PC} - L_G*V_x*B_z$ (kV)	Φ_V (0 B_z method) (kV)	Φ_V (extrapolation method) (kV)
-7.5	-400	5	6.7	128.0	153.1	25.1	27.2	24.6
-15	-400	5	5	191.1	207.3	26.2	27.2	24.6
-7.5	-400	10	6.4	122.3	156.1	33.8	33.0	26.1
-15	-400	10	5	191.1	228.6	36.5	33.0	26.1
-15	-800	5	2.5	191.1	255.0	64.1	58.6	57.4

Even though the solar wind B_z, velocity, and density cover a range of values, each row shows a fairly consistent clustering of Φ_V values. Comparisons for most pairs of viscous potential values, for the same solar wind conditions, are within about 10% of each other. The extreme cases include one streamline value exceeding the comparable extrapolation value by 30% (of the extrapolation value, which is smaller) and another reaching almost 40%. Sometimes all three values are close to each other, but in the cases with the largest range of values, the zero B_z values are intermediate between the more extreme values. Thus, since none of these methods are definitive, we will be using only the zero IMF method for the remainder of this work.

CHAPTER 3

VARIABLES FOUND TO AFFECT THE VISCOUS POTENTIAL IN LFM

In this chapter, several factors are examined which affect the viscous potential in LFM, as well as one factor that does not at this time seem to have any effect. An equation is produced which predicts the viscous potential when solar wind conditions are provided.

Here is a table of viscous potential values found for a range of solar wind density and velocity (V_x) values, using the "zero B_z" method described in Section 2.3, with ionospheric Pedersen conductivity (Σ_P) set to 10 mhos, as explained in Section 2.1.

Table 3-1. Viscous potential values (in kV) for a variety of solar wind velocity and density values.

		Solar wind velocity					
		-300 km/s	**-400 km/s**	**-500 km/s**	**-600 km/s**	**-700 km/s**	**-800 km/s**
Solar wind density	**1 cm^{-3}**	7.9	11.7	18.3	23.4	26.3	31.3
	5 cm^{-3}	18.0	27.2	31.8	39.6	52.5	59.4
	8 cm^{-3}	22.3	29.4	39.5	53.2	59.7	92.9
	10 cm^{-3}	25.2	33.0	47.4	57.7	71.9	85.6
	15 cm^{-3}	29.0	39.0	51.1	66.8	90.9	109.4

3.1 Solar wind velocity

Figure 3-1 plots the rows from Table 3-1, showing how the viscous potential changes with changes in the solar wind velocity, from V_x = -200 km s^{-1} up to V_x = -800 km s^{-1}, but holding density constant. Values found from the same solar wind density are connected by lines. There is a clear increasing trend in Φ_V as V_x increases, but the increase is faster than linear. To find the exponent of a non-linear trend, we plot the same data on a $\log_{10}$-$\log_{10}$ plot, as seen in Figure 3-2, then add a linear fit to each dataset. In this type of plot, the slope of the linear fit for each series of data gives the exponent for that series from Figure 3-1. The exponents range from 1.202 to 1.434, with no clear trend as density changes. The average of the five values is 1.33, with a standard deviation of 0.084.

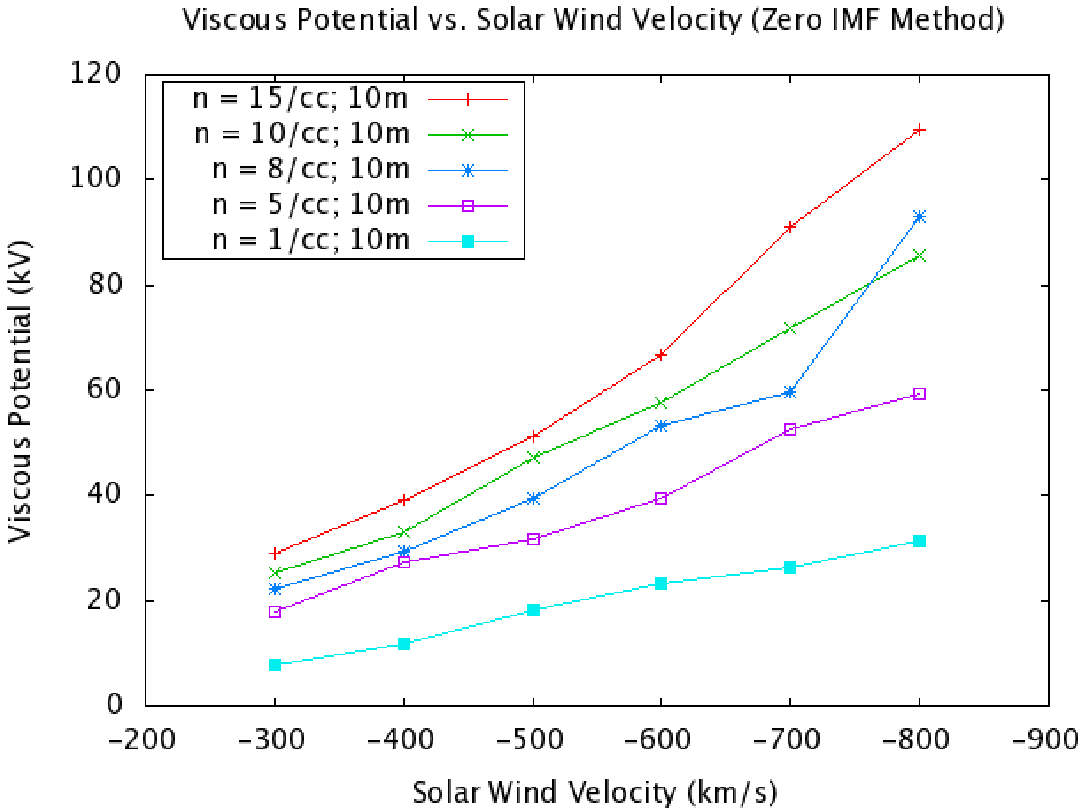

Figure 3-1. Viscous potential for constant solar wind density, varying solar wind velocity. [From *Bruntz et al.*, 2012a.]

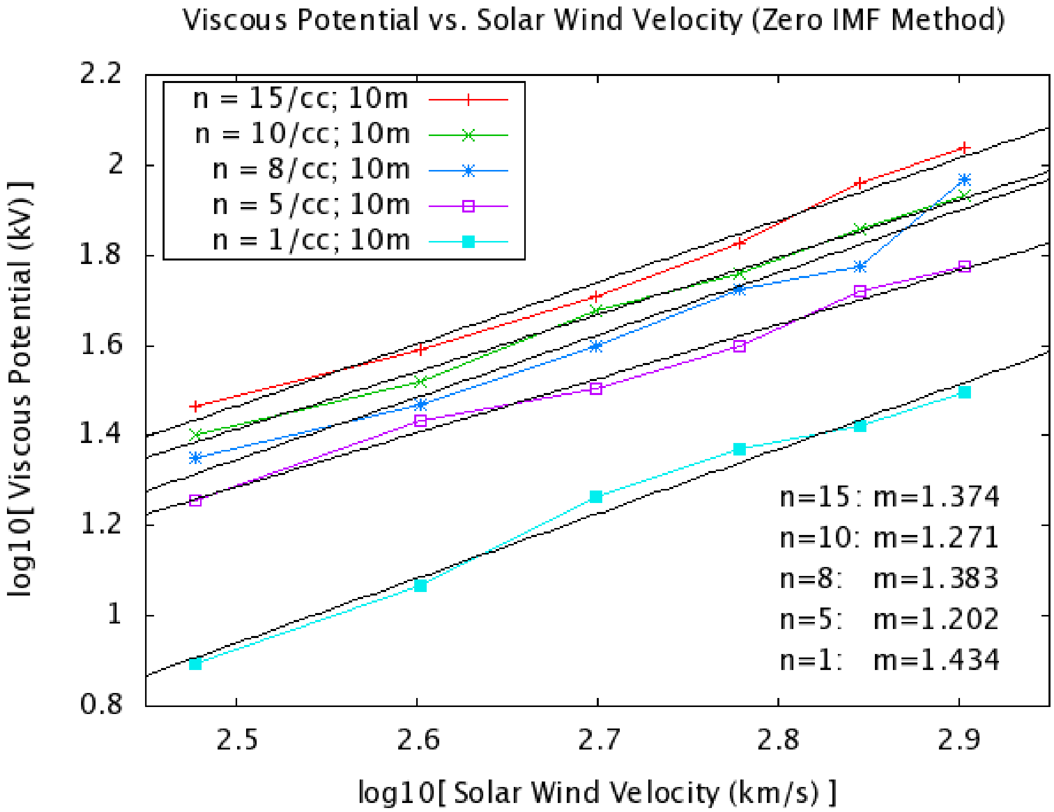

Figure 3-2. A $\log_{10}$-$\log_{10}$ plot of the data in Figure 3-1.
[From *Bruntz et al.*, 2012a.]

3.2 Solar wind density

Figure 3-3 shows a plot of the columns in Table 3-1, showing how the viscous potential changes with changes in the solar wind density, from n = 1 cm^{-3} up to n = 15 cm^{-3}, but holding solar wind velocity constant.

Values found from the same solar wind velocity are connected by lines. There is a clear increasing trend in Φ_V as n increases, but the increase is less than linear. To find the exponents, we again plot the same data on a $\log_{10}$-$\log_{10}$ plot, as seen in Figure 3-4, then add a linear fit to each dataset. The slopes of the linear fits for each series give the exponent for each series from Figure 3-3. The exponents range from 0.389 to 0.490, again with no clear trend as velocity changes. The average of the six values is 0.439, with a standard deviation of 0.0347.

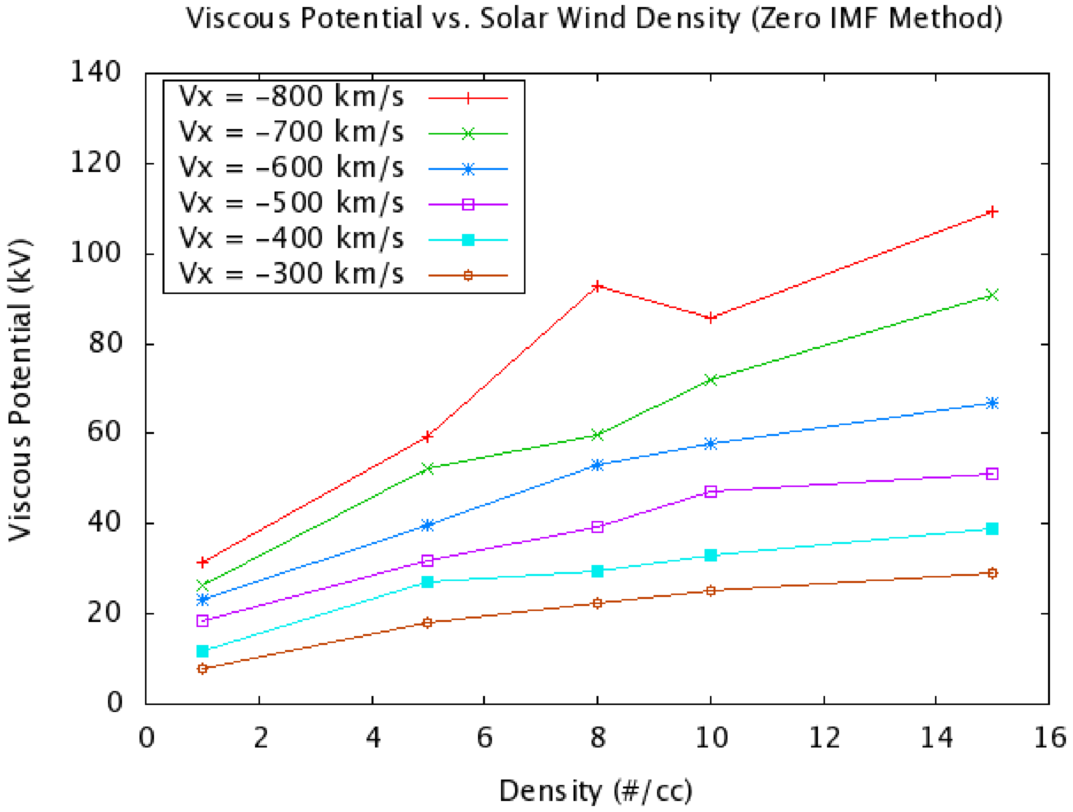

Figure 3-3. Viscous potential for constant solar wind velocity, varying solar wind density. [From *Bruntz et al.*, 2012a.]

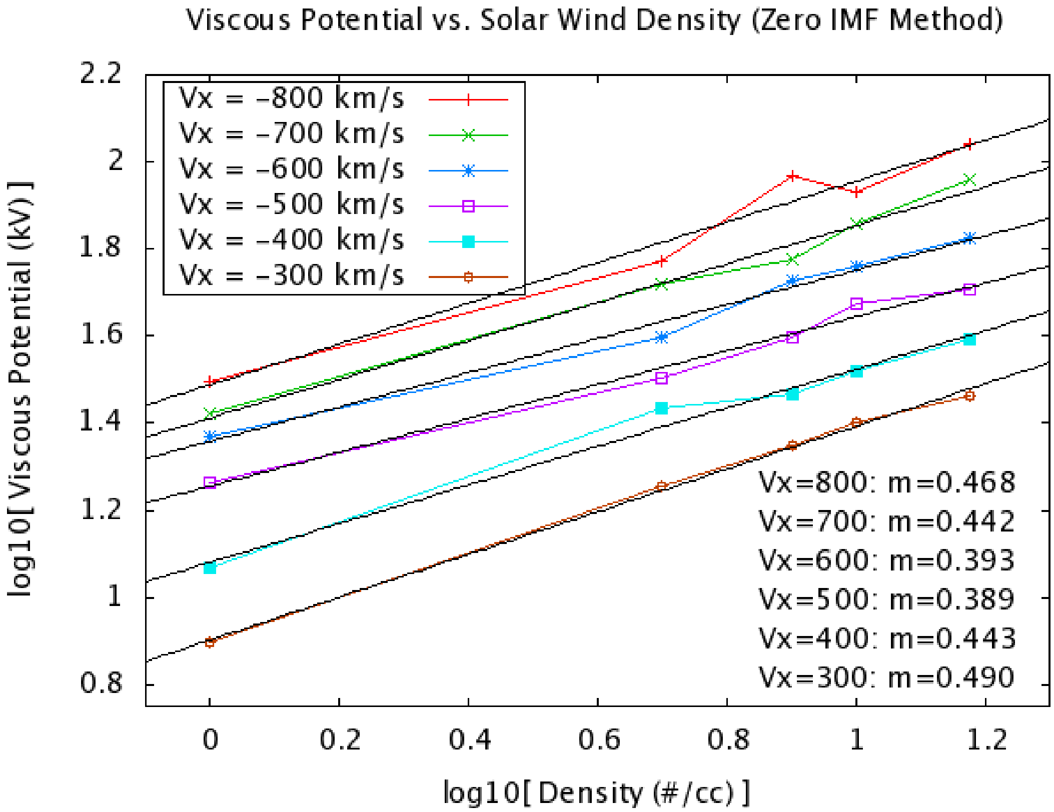

Figure 3-4. A $\log_{10}$-$\log_{10}$ plot of the data in Figure 3-3.
[From *Bruntz et al.*, 2012a.]

3.3 Ionospheric conductivity

We also tested the viscous potential for a variety of ionospheric Pedersen conductivity values, using standard solar wind conditions (n = 5 cm^{-3}, V_x = -400 km s^{-1}, B_z = 0 nT). *Lopez et al.* [2010] predicted that there would be an inverse relationship between conductivity and the viscous potential, and showed some limited results supporting that prediction in LFM results. The theory behind the idea is that the velocity shear in magnetospheric viscous cells also produces a magnetic shear, since the plasma and field are tied together. That magnetic shear is transmitted to the ionosphere through field-aligned currents [*Sonnerup*, 1980]. A lower conductivity in the ionosphere makes it "stiffer," and thus requires a higher potential to match the current driven by the viscous interaction. Fuller support for this prediction is presented in Table 3-2 and plotted in Figure 3-5. The data show a clear inverse relationship between Φ_V and Pedersen conductance, which is further explored in Figure 3-6, which plots $(1/\Phi_V)$ vs. Pedersen conductance. A linear fit to those data shows a very high correlation coefficient: $R^2 = 0.991$. Inverting the formula for the fit to the data produces an equation for Φ_V as a function of Σ_P:

$$\Phi_V = (0.002\times\Sigma_P + 0.019)^{-1} \text{ (in kV)}$$

Equation 2

This implies that in the low extreme of conductivity (0 mhos – which is unlikely, if not impossible), Φ_V could go as high as 50 kV, or for extremely high conductivity, Φ_V would drop to virtually 0 kV, all with the same solar wind conditions. Unfortunately, it is extremely difficult to measure ionospheric conductivity directly; combined with the difficulty in any sort of direct measurement of the viscous potential, any empirical support for these conductivity results may be a long way off.

Table 3-2. Viscous potentials for various ionospheric Pedersen conductances (standard solar wind conditions).

Pedersen Conductivity (mhos)	1	2.5	5	7.5	10	12.5	15	20	25	30
Φ_V (kV)	42.7	38.2	36.1	32.0	27.2	22.6	20.3	16.8	14.1	12.9

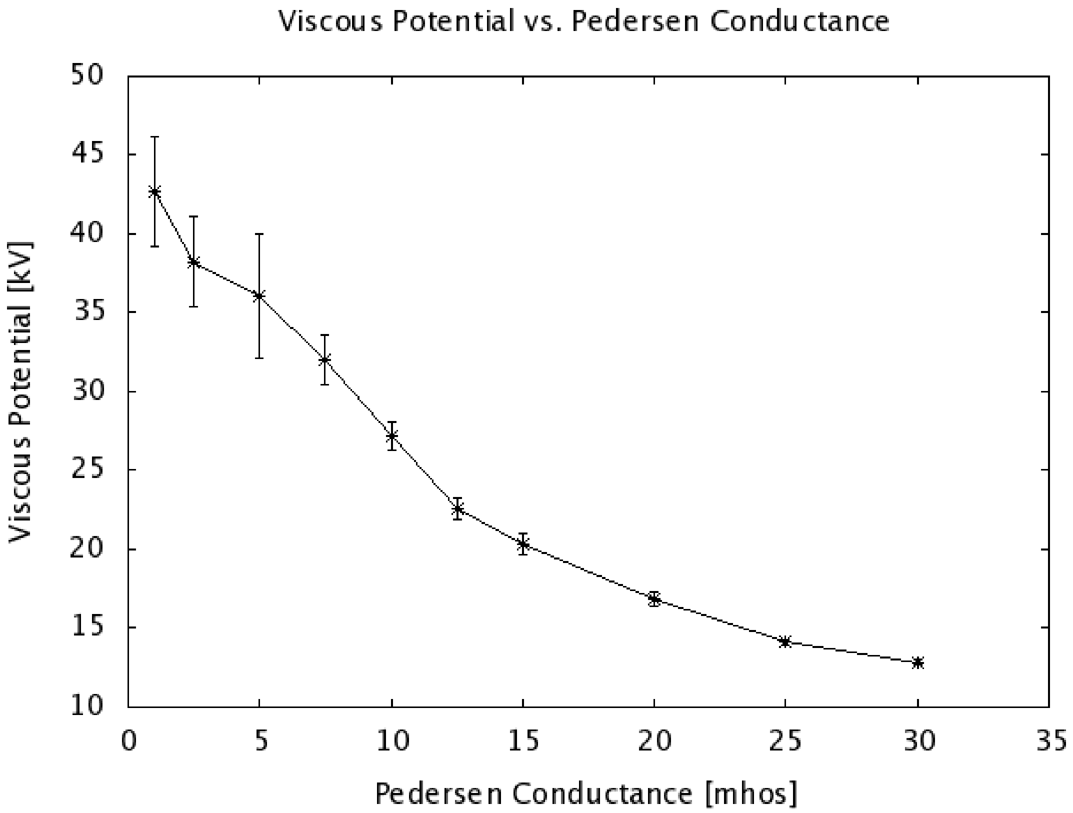

Figure 3-5. Viscous potential for various Pedersen conductances, from data in Table 3-2. [From *Bruntz et al.*, 2012a.]

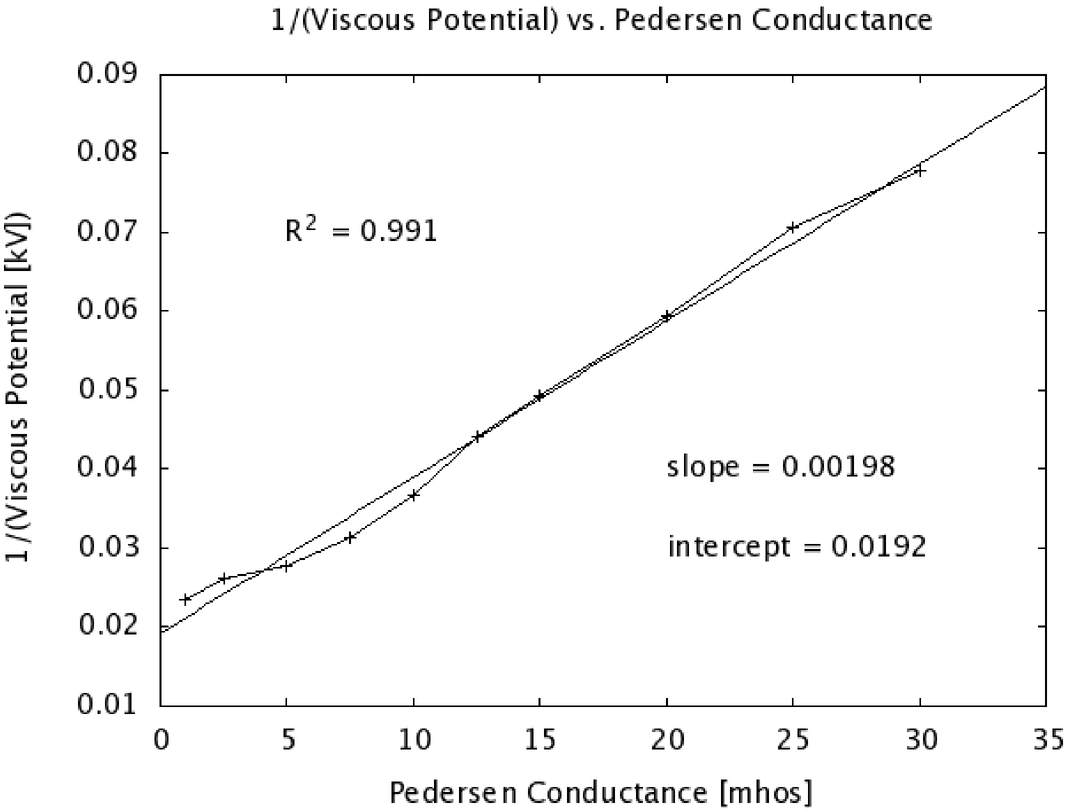

Figure 3-6. Plot of data in Figure 3-5, plotted as (1/VP) vs. Pedersen conductance.
[From *Bruntz et al.*, 2012a.]

3.4 A note on B_z dependence

After seeing that the viscous potential is a function of solar wind density, solar wind velocity, and ionospheric Pedersen conductivity, it might be natural to ask whether Φ_V might also be dependent on solar wind magnetic field, as well. The answer at this point is a definite “probably not.” The strongest argument against a B_z dependence comes from *Lopez et al.* [2010], Figure 7, which is presented below as Figure 3-7. In this figure, Φ_{PC} has been calculated by two different methods, then plotted against solar wind VB_z; since V was constant for these runs, that factor does not affect the results.

The first method simply finds Φ_{PC} from the LFM ionosphere, without concern for the Φ_R and Φ_V components. The second method calculated Φ_V using the extrapolation method, then uses the streamline analysis to find Φ_R, then adds the two together to get Φ_{PC}. If Φ_V had a B_z-dependence, then the composite Φ_{PC} would become increasingly larger or smaller than Φ_{PC} from the ionosphere, since the ionospheric Φ_{PC} would incorporate the variable Φ_V as B_z increased, whereas the composite Φ_{PC} uses a constant Φ_V. Yet looking at the plot, the two datasets are remarkably close to each other throughout the range of B_z. If there is any effect, it might be that Φ_V increases with increasing B_z, since the composite Φ_{PC} tends to be slightly smaller than Φ_{PC} from the ionosphere when the two differ – but that effect could also be random variability in the data.

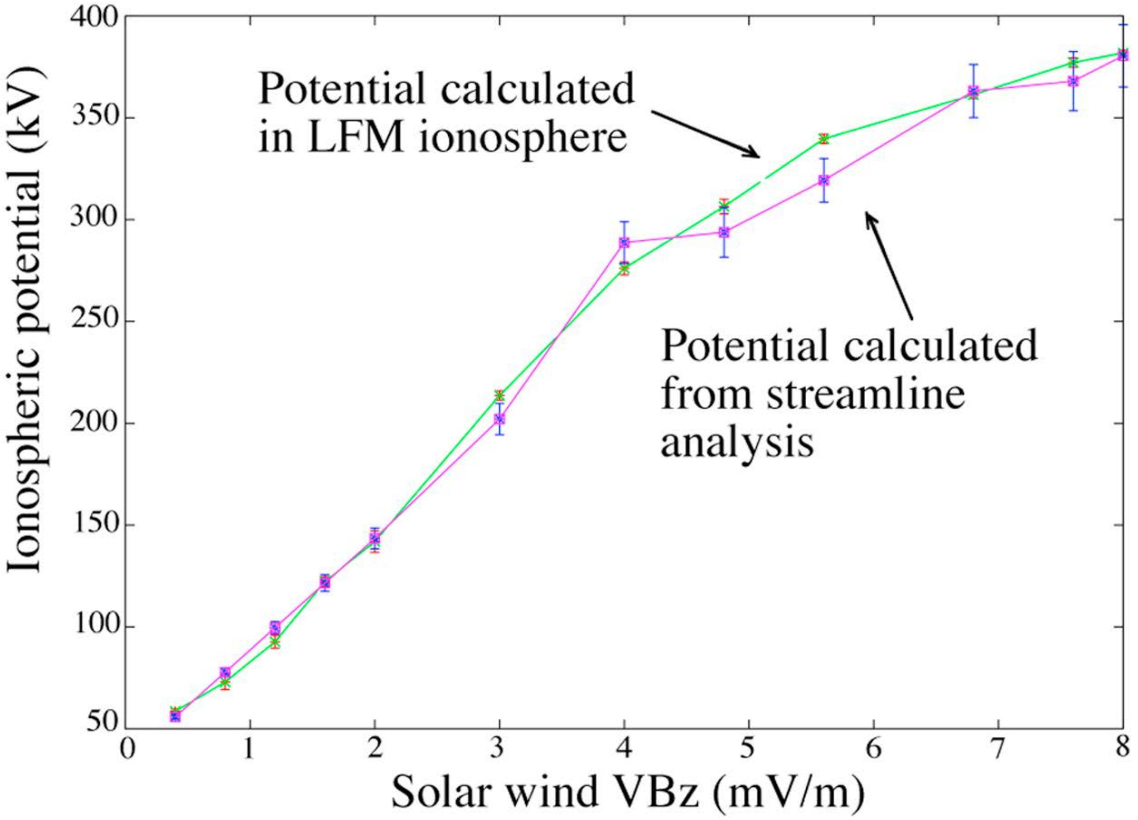

Figure 3-7. Cross-polar cap potential vs. VB_z, calculated by two different methods. [From *Lopez et al.*, 2010,.]

Another way of looking for a B_z-dependence is through the data in Table 2-1. Column 7 gives Φ_V based on the streamline analysis method, while column 8 gives Φ_V from the zero B_z method. Using these data, we can create two series of three Φ_V datapoints, with constant solar wind velocity and density, and B_z = 0, -7.5, and -15 nT, plus one series of two Φ_V datapoints for B_z = 0 and -15 nT. Any B_z dependence should show up as a trend in Φ_V, as plotted in Figure 3-8, along with linear fits to the data. Looking at the data, though, we see that there is no strong evidence for a trend. For the three n = 5 cm^{-3}, V_x = -400 km s^{-1} datapoints, Φ_V first drops significantly, then rises slightly. For the three n = 10 cm^{-3}, V_x = -400 km s^{-1} datapoints, Φ_V rises throughout, but by a very small amount – about 10% over a range of 15 nT (which is a significant range in the IMF). For the two $n = 5$ cm^{-3}, $V_x = -800$ km s^{-1} datapoints, Φ_V again rises, but again only by about 10% over a range of 15 nT.

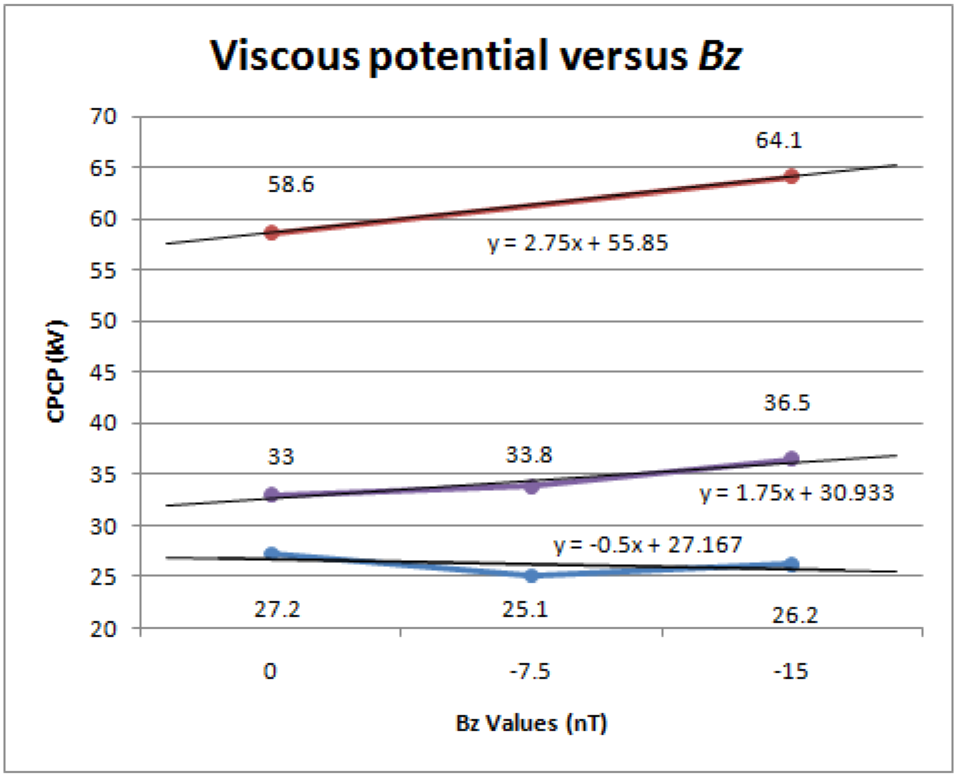

Figure 3-8. Three series of viscous potential data (constant conditions) versus B_z. Datapoint values and linear fits are shown, as well.

So in the final analysis, there is no clear indication of a B_z dependence in Φ_V. Our data do not preclude such a possibility, and most of the data hint that such a dependence would be of the form of an increase in Φ_V as B_z becomes more negative. But our data are clear that any such dependence would have to be very small, and such a small signal is currently beyond our ability to easily and reliably draw out. (It would probably take a skilled person dozens of hours to collect enough data using the streamline method to make any confident statements. Such a large investment for such a small *possible* payoff is simply not warranted for the current project.)

3.5 A formula for the viscous potential in LFM, incorporating velocity and density

We can combine the results of the velocity and density dependence into a predictive formula for the viscous potential as follows. We take the following equation as the form of an equation to calculate the viscous potential:

$$\Phi_V = \delta n^{\alpha} V^{\beta}$$

Equation 3

where Φ_V is the unknown viscous potential, which is equal to an unknown density *n* raised to a power α multiplied by an unknown velocity *V* raised to a power β multiplied by an unknown proportionality constant δ. We now repeat the equation with known values:

$$\Phi_{V0} = \delta n_0^{\alpha} V_0^{\beta}$$

Equation 4

where n_0 andV_0 are known values that produce a known viscous potential Φ_{V0}, and δ is still an unknown constant. Dividing Equation 3 by Equation 4, moving Φ_{V0} to the right hand side, and cancelling δ yields:

$$\Phi_V = \Phi_{V0}(n/n_0)^{\alpha}(V/V_0)^{\beta} = \mu n^{\alpha} V^{\beta}$$

Equation 5

where $\mu = \Phi_{V0}(1/n_0)^{\alpha}(1/V_0)^{\beta}$. Using $\alpha = 0.439$ from Section 3.2 and $\beta = 1.33$ from Section 3.1, μ becomes a constant that depends on a reference set of solar wind velocity and density values and the corresponding viscous potential, from Table 3-1. We chose $n_0 = 8\ \mathrm{cm}^{-3}$ and $V_0 = 600\ \mathrm{km\ s}^{-1}$, which corresponds to $\Phi_{V0} = 53.2$ kV. This yields $\mu = 0.00431$ (units omitted), which can be substituted into Equation 5, along with the values of α and β to produces the equation

$$\Phi_V = (0.00431)n^{0.439}V^{1.33} \text{ (in kV)}$$

Equation 6

This equation can be used to find realistic viscous potential values for any solar wind density and velocity combination. We will refer to it, when necessary, as the "Bruntz et al. viscous potential formula". (This equation and a brief form of the derivation were first published in *Bruntz et al.* [2012a].)

We can plot the 30 values of Φ_V found by LFM and listed in Table 3-1 versus the Φ_V values predicted by Equation 6 for the same solar wind conditions, to see how accurate the equation is. These data are plotted in Figure 3-9. The predicted values match the measured values extremely well – the correlation coefficient is $R^2 = 0.9795$. While it might not at first seem surprising that a dataset would match well against predictions from a formula derived from those same data, this level of accuracy was by no means guaranteed, especially over such a large range of input values (density from 1 cm^{-3} to 15 cm^{-3} and velocity from -300 $\mathrm{km\ s}^{-1}$ to -800 $\mathrm{km\ s}^{-1}$).

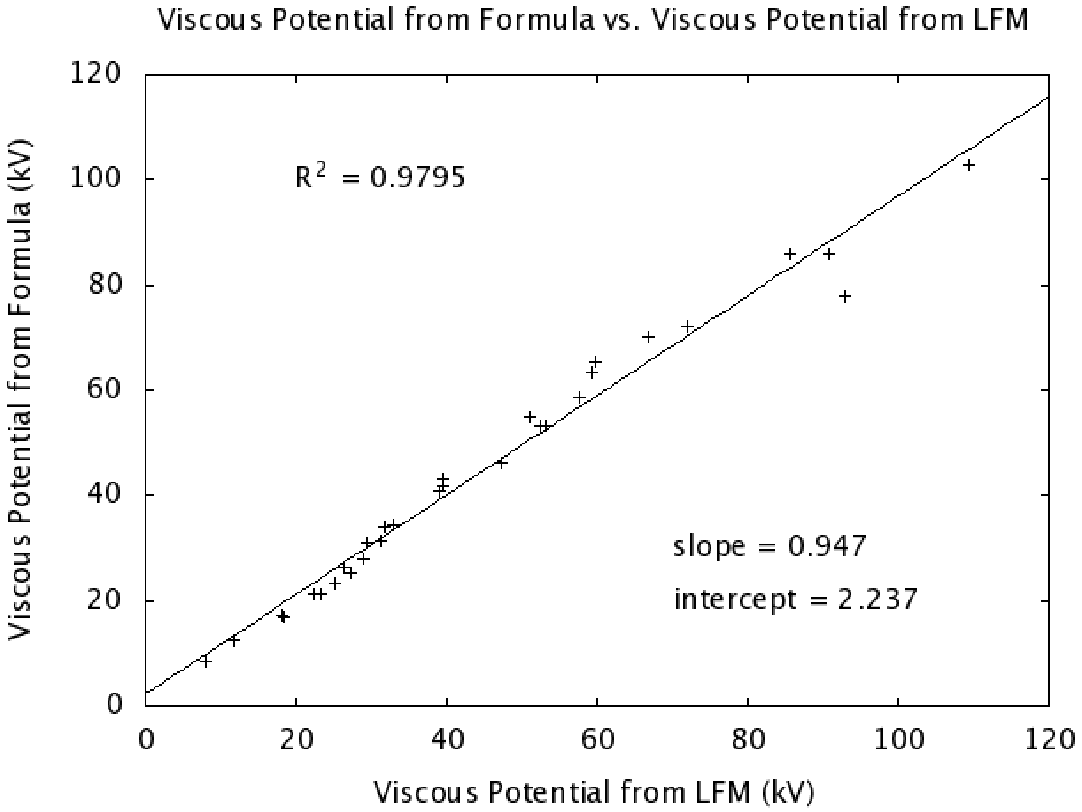

Figure 3-9. Plot of viscous potential values measured in LFM runs (Table 3-1) versus viscous potential values predicted by Equation 6.

CHAPTER 4

COMPARISON WITH OTHER RESULTS

4.1 Comparison with an empirical scaling factor for the viscous interaction

4.1.1 The Newell et al. [2008] viscous scaling factor

Newell et al. [2008] tested a variety of coupling functions for the viscous interaction using ten magnetospheric characterizations, such as geomagnetic indices and magnetic cusp latitude (though Φ_{PC} was not one of them). They found that $n^{1/2}V^2$ performed best (out of 20 candidate functions) in accounting for some of the variance in the data. This result only gives the form of the response of the viscous interaction to changes in solar wind density and velocity; it does not return a potential due to the viscous interaction – though it is reasonable to expect that the viscous potential would follow the same scaling as the viscous coupling function. As the most recent and most mathematically detailed empirical characterization of the viscous interaction, it is likely to provide the most fruitful comparison to our semi-empirical (i.e., derived from simulation results) viscous potential formula.

4.1.2 Comparing the Newell et al. and the Bruntz et al. viscous scaling factors

In comparing the functional form of the Bruntz et al. viscous potential formula and the *Newell et al.* [2008] viscous coupling function, it is convenient to represent both as $n^{\alpha}V^{\beta}$. In this form, the Bruntz et al. values are $\alpha = 0.439$, $\beta = 1.33$, while the Newell et al. values are $\alpha = 0.5$, $\beta = 2$. Both are sub-linear in n and supra-linear in V. The Newell et al. function, however, increases faster for both variables than the Bruntz et al. function, as can be seen in Figure 4-1 and Figure 4-2.

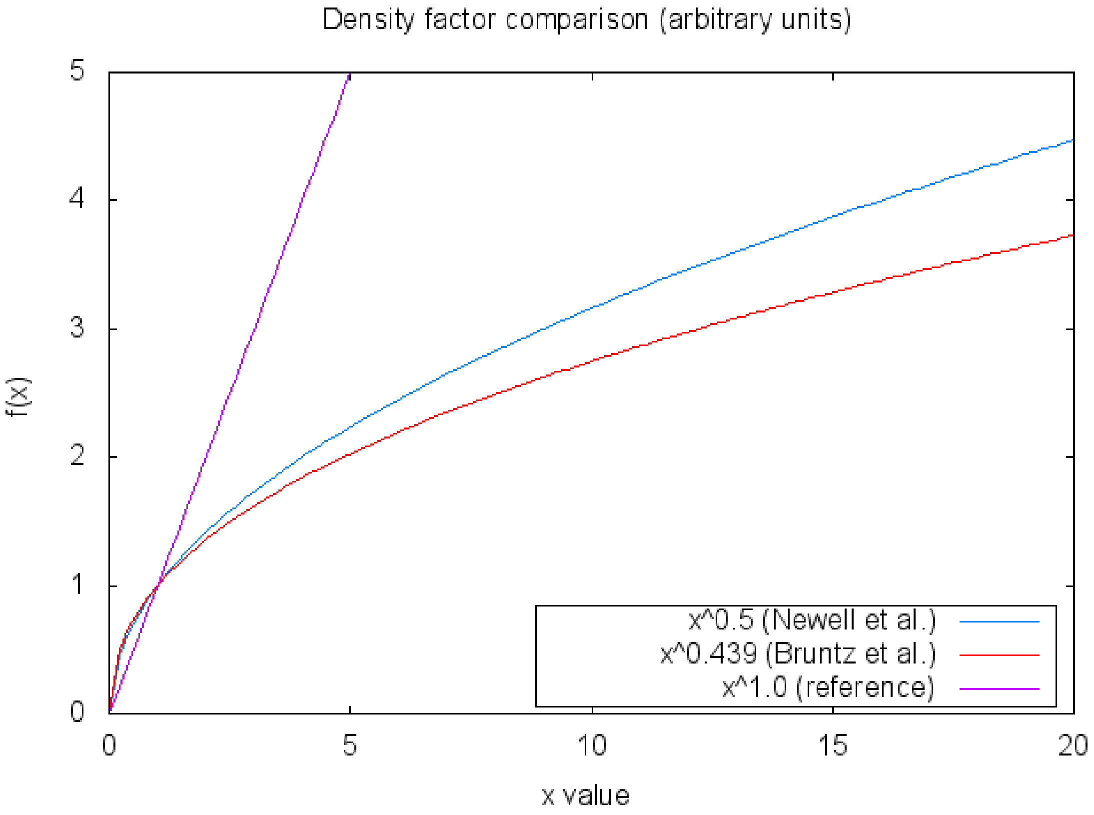

Figure 4-1. Comparison of the density factor in the Newell et al. and Bruntz et al. viscous scaling functions.

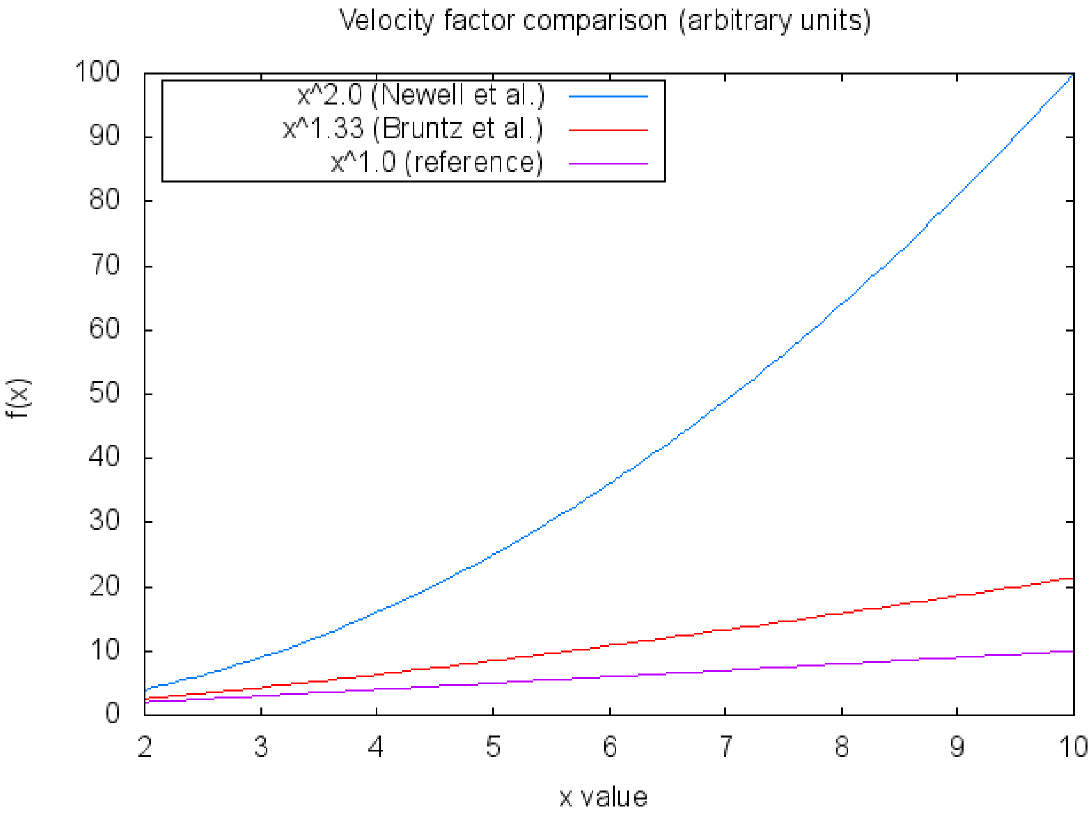

Figure 4-2. Comparison of the velocity factor in the Newell et al. and Bruntz et al. viscous scaling functions.

One result of this difference in scaling is that the value returned by the Newell et al. scaling factor will increase or decrease by more than the Bruntz et al. scaling factor, for the same change in solar wind conditions. As an example, going from the lowest density and velocity values in Table 3-1 (n = 1 cm^{-3}, V = 300 km s^{-1}) to the highest (n = 15 cm^{-3}, V = 800 km s^{-1}), the value of the Bruntz et al. scaling factor increases by a factor of 12.1. The value of the Newell et al. scaling factor increases by a factor of 27.5 for the same change in solar wind conditions – more than twice the increase shown by the Bruntz et al. scaling factor.

Examining the values of α and β more closely, we note that *Newell et al.* [2008] tested a list of 20 candidate viscous coupling functions, which were all functions of solar wind density, velocity, and pressure. Table 2 in that paper ranks the relative success of the different viscous coupling functions at accounting for variations in the magnetospheric variables (which were also dependent on reconnection, so the viscous interaction was not expected to account for all of the variation). The most successful, of course, was $n^{1/2}V^2$, accounting for 22.3% of the variation, but the second most successful was $n^{1/3}V^2$, at 21.8%. In terms of $n^\alpha V^\beta$, α for the Bruntz et al. viscous coupling function is between the most successful and second-most successful functions from the *Newell et al.* [2008] list: $0.333 < 0.439 < 0.5$. For β, in the *Newell et al.* [2008] list, the two best-performing functions contained $\beta = 2$, but the list did not have any functions of the form $n^\alpha V^\beta$ with $\beta < 2$ (except for the trivial and dismally-performing nV); whereas the Bruntz et al. function has $\beta = 1.33 < 2$.

The implications of these relations can be drawn more clearly from Figure 4-3, where we see that the two most successful α-β pairs from *Newell et al.* [2008] are also the two that are closest to the Bruntz et al. α-β pair. It is possible that best Newell et al. function is not <u>at</u> a local maximum, but rather <u>near</u> a local maximum, and that the Bruntz et al. function might be even nearer to that maximum, in the undersampled region of $\beta < 2$.

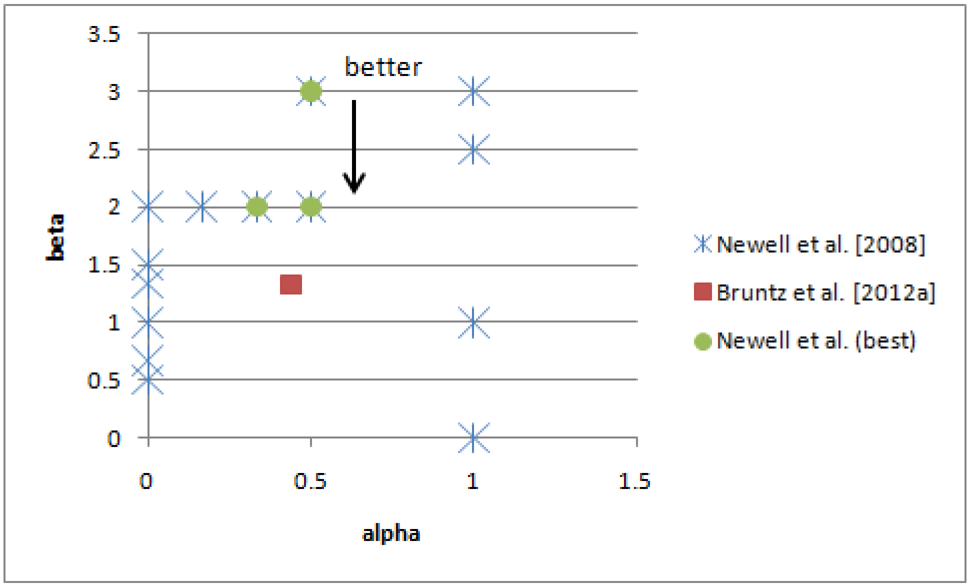

Figure 4-3. Plots of alpha-beta pairs in *Newell et al.* [2008] and *Bruntz et al.* [2012a].

4.2 Comparison with an LFM run performed with real solar wind data

For further testing of the Bruntz et al. viscous potential formula, we performed several LFM runs with real solar wind data and specific modifications of that data. The modification discussed here was chosen to reveal what portion of Φ_{PC} from the full run was contributed from Φ_V, so that that portion could be compared to the Bruntz et al. formula. We performed several other comparisons to the LFM runs, as well, using other viscous potential formulae and Φ_{PC} from an empirical model.

4.2.1 Overview of the Whole Heliosphere Interval

The period we chose to analyze was the Whole Heliosphere Interval (WHI): Carrington Rotation 2068, which lasted from 20 March 2008 (DOY (Day of Year) 87) through 16 April 2008 (DOY 107). The WHI was planned in order to improve our understanding of the Sun and the heliosphere through intensive and coordinated observations and modeling [e.g., *Gibson et al.*, 2009]. The previously-mentioned Center for Integrated Space Weather Modeling (CISM) used several models that it has helped develop, to simulate the WHI, with a number of papers being published in a special issue of the Journal of Atmospheric and Solar-Terrestrial Physics (JASTP), including the WHI-related research presented here (in *Bruntz et al.* [2012b]; others include *Lopez et al.* [2012], and *Wiltberger et al.* [2012], both of which have ties to this work, and vice-versa).

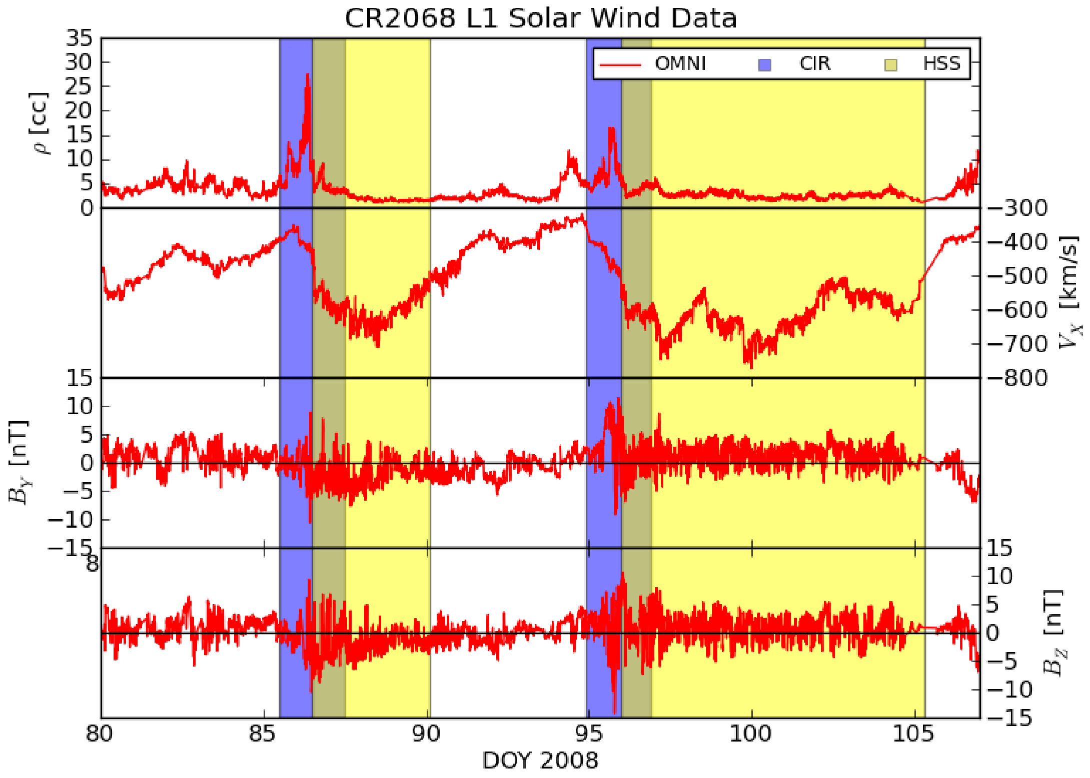

Figure 4-4. Components of the solar wind during the WHI.
[From *Bruntz et al.*, 2012b.]

Figure 4-4 shows the most pertinent components of the solar wind during the WHI, taken from the OMNI database of solar wind data, and plotted in the GSM coordinate system. Worth noting are the two blue bands, marking co-rotating interaction regions (CIRs) in the solar wind, starting on DOY 85 and the end of DOY 94, in which high speed solar wind pushes the slower wind ahead of it, similar to a snowplow – note the observed increase in solar wind mass density (ρ) as the CIRs pass Earth. The two yellow regions after the CIRs are the high speed streams (HSSs) themselves, which drive the CIRs. The increased speed is noticeable in the panel with V_x, but notice that V_x is negative away from the Sun, so speed past the Earth increases toward the bottom of that panel, not the top. The IMF components B_y and B_z also show larger amplitudes during both the CIR and the indeterminate time period between the CIR and the HSSs (grey), which may belong to either the CIR or the HSS. Just as the CIR piles up solar wind plasma, it also piles up the magnetic field, increasing the components transverse to its direction of motion.

4.2.2 Full solar wind run and zero IMF run

We ran the standard LFM code with the full solar wind input file for the WHI, using the empirical ionosphere and an F10.7 value of 74 SFU (solar flux units), which is the average for the WHI interval. This setup matched a run of the CMIT (Coupled Magnetosphere-Ionosphere-Thermosphere) model, run by Wiltberger et al. CMIT [*Wiltberger et al.*, 2004; *Wang et al.*, 2004] uses the LFM code, coupled to the Thermosphere-Ionosphere Nested Grid (TING) model, which provides a more detailed model of the Earth’s ionosphere. Comparing the results of the CMIT and stand-alone LFM models (the top two panels in Figure 4-5) verifies that the outputs are largely the same. More detailed analysis found that Φ_{PC} from the two runs tended to differ slightly in some of the large Φ_{PC} spikes, but those regions are not important for this study. Verifying that the two runs produce similar enough results was important because our lab can run LFM locally, on our own computers, whereas we do not currently have the capability of running CMIT locally. We would have had a much harder time running the multiple specially-modified runs that we needed for this and some other studies, but these results show that none of the essential physics for this study are lost by running LFM alone, rather than CMIT.

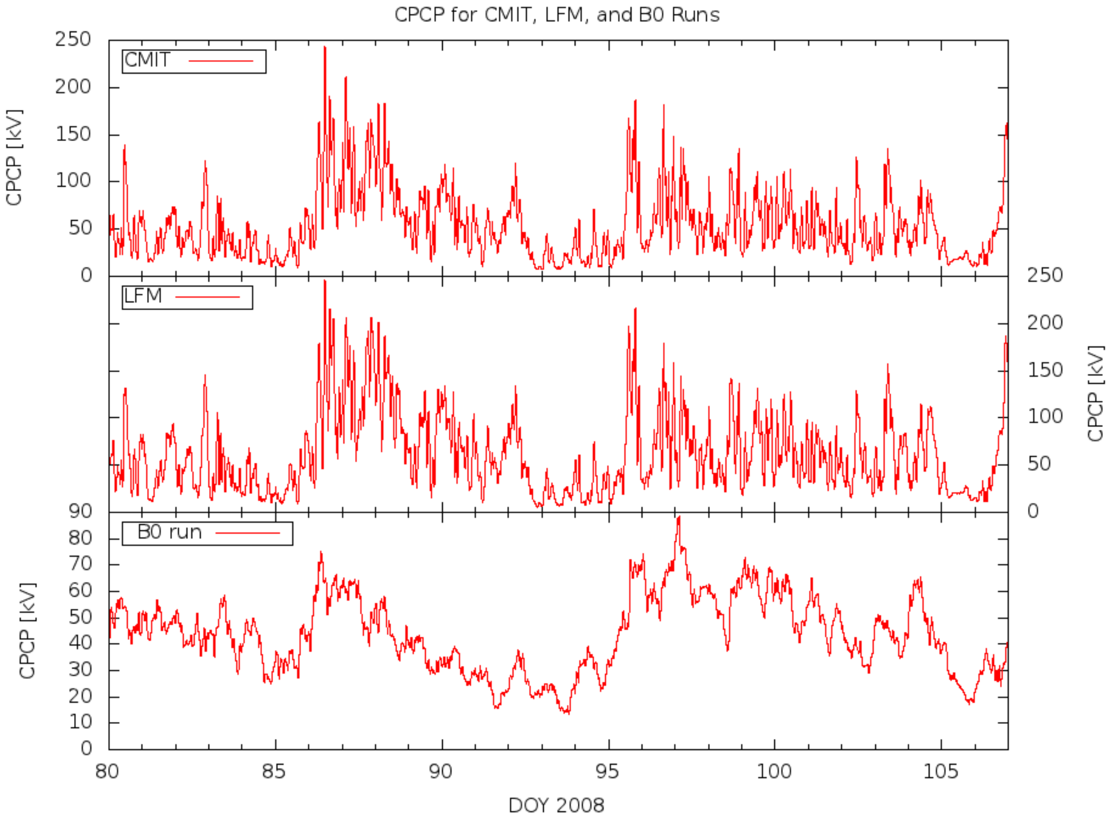

Figure 4-5. CPCP for the CMIT run, the stand-alone LFM run with full solar wind, and the stand-alone LFM run with zero IMF ("B0"). Note that the scale on the B0 run is different. [From *Bruntz et al.*, 2012b.]

In addition to the full solar wind LFM run, we performed another LFM run in which we set all of the IMF components in the WHI solar wind file to zero (thus the term "B0 run"); all other aspects of the solar wind file and the LFM setup were identical. The CPCP values for the B0 run are shown in the third panel of Figure 4-5. In this run, the entire CPCP is a product of the viscous interaction, since there is no IMF to reconnect with Earth's magnetic field. The CPCP values from the two runs are overplotted in Figure 4-6 for easier comparison.

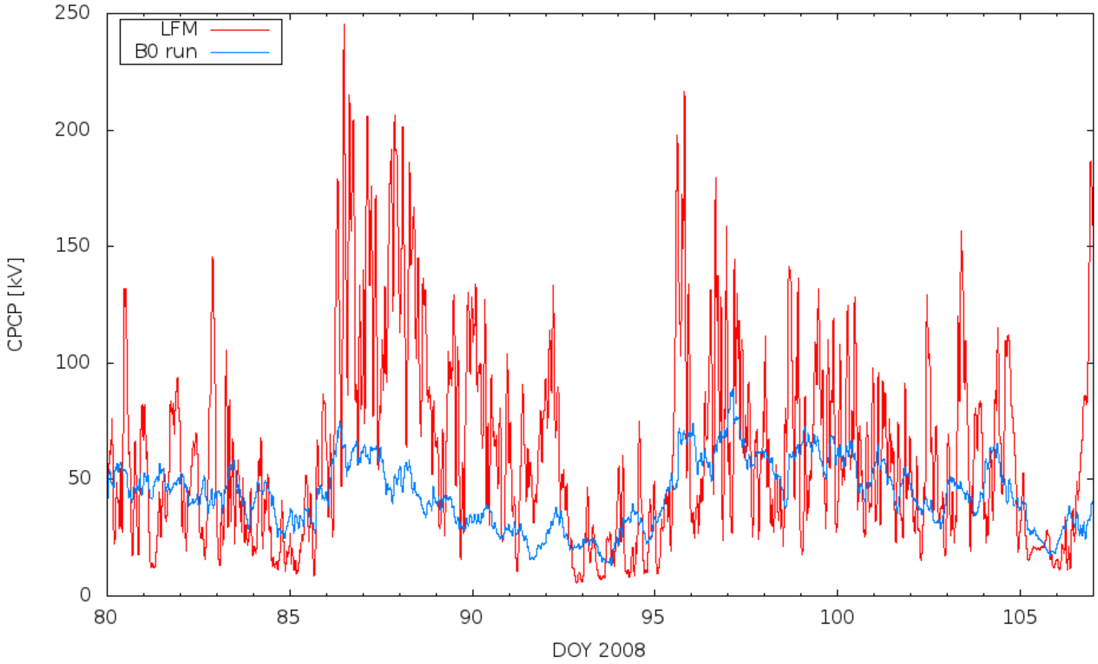

Figure 4-6. CPCP for the full-solar wind LFM run and the zero-IMF LFM run, for the entire WHI interval. [From *Bruntz et al.*, 2012b.]

One feature of Figure 4-6 that might at first seem puzzling is that there are numerous time intervals in which the LFM potential actually drops lower than the B0 potential. This has been explained by a recent discovery by Shree Bhattarai and Ramon E. Lopez [*Bhattarai et al.*, 2012; *Lopez et al.*, 2012] which has found that the viscous interaction, and thus the viscous potential, is reduced with increasing northward B_z (though as discussed in Section 3.4, the viscous potential stays constant for southward B_z). This is shown clearly for the WHI in *Lopez et al.* [2012], in which it is shown that the periods in which the LFM CPCP is lower than the B0 CPCP all correspond to periods of prolonged northward B_z (Figure 3 in that paper). The explanation suggested in that paper involves the different polar cap potential distribution for northward B_z. As discussed in Section 1.4, for southward B_z, the idealized polar cap has two circulation cells, with the cell due to the viscous interaction nested inside the cell due to reconnection (Figure 1-8), and the potentials from the two processes add together to form the cross-polar cap potential ($\Phi_{PC} = \Phi_{max} - \Phi_{min}$). For northward B_z however, the viscous and reconnection cells are separated into a four-cell pattern [e.g., *Burke et al.*, 1979] and do not add together. Instead, the largest positive potential will be found either in one of the viscous cells or in one of the reconnection cells, with the other positive cell making no contribution to the CPCP, and likewise for the largest negative potential; the larger potential of each polarity essentially “eclipses” the smaller potential of the same polarity. This is shown in Figure 4-7, in which the outer peaks, from the viscous potential, are seen to shrink as northward B_z increases, from panel a-d, while the inner peaks, from reconnection, grow. In panels a-c, the viscous potential exceeds the reconnection potential, and so is the sole source for the CPCP; in panel d, the reconnection potential has grown enough that it now eclipses the still-shrinking viscous potential, and so it is now the sole source for the CPCP. For most of the WHI, the reconnection potential is smaller than the viscous potential, so measurements of the CPCP for northward B_z are usually measurements of the (reduced) viscous potential [*Lopez et al.*, 2012]. The physical reason suggested in that paper for the reduced viscous potential is that unlike southward B_z, northward B_z produces sunward plasma flow across the center of the polar cap, and that the return flow from that convection must flow antisunward just outside the magnetopause. Thus, the antisunward flow provides a buffer between the quiescent magnetospheric plasma and the fast-moving magnetosheath plasma. This reduces the velocity shear at the magnetopause, which reduces the viscous interaction and thus the viscous potential.

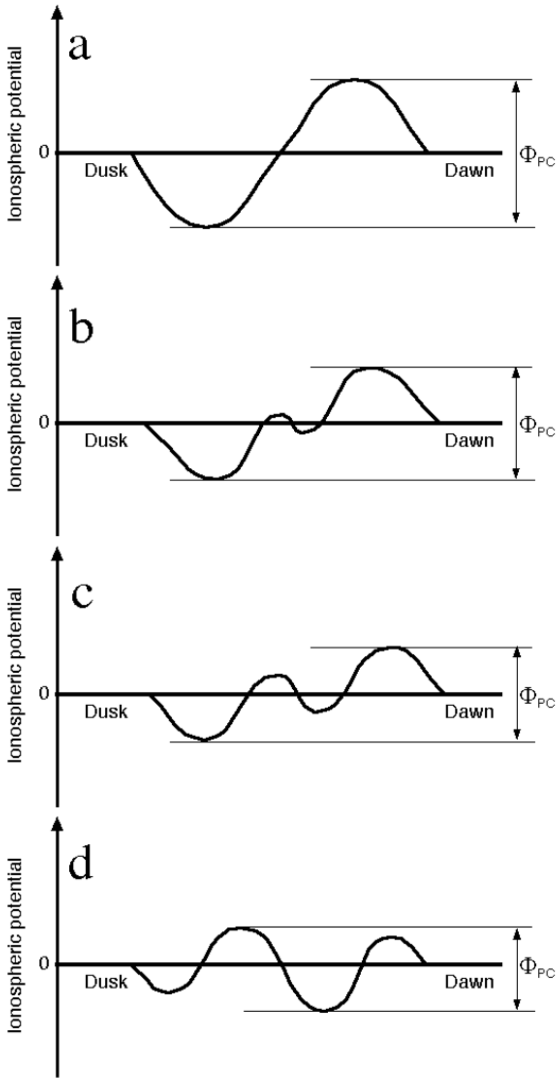

Figure 4-7. How the CPCP is formed for northward B_z. In panels a-c, the viscous potential alone determines the CPCP; in panel d, the reconnection potential alone determines the CPCP. [From *Lopez et al.*, 2012.]

For southward B_z, though, (when the viscous and reconnection potentials add) there are many times when the CPCP from the B0 run is a significant fraction of the CPCP from the full-IMF LFM run. The WHI has numerous extended-northward B_z

periods, but is unfortunately very sparse when it comes to uninterrupted southward B_z periods. This comes into play in that northward B_z reduces the viscous potential, and so any average of the full-IMF LFM CPCP over a period with northward B_z will have a reduce average value, thus exaggerating the importance of the viscous potential. We can find a few short periods, though, and look at the peak potentials.

Figure 4-8 shows the CPCP for the full-IMF LFM and zero-IMF B0 runs for DOY 85-90, along with the IMF B_z value. Note that the B_z value is plotted with the same numerical values (the scale on the left side) as the CPCP values, but different units (nT for B_z, versus kV for CPCP); the main purpose is to show B_z polarity – north or south – and general magnitude. Also note that the CPCP values (but not the B_z values) have been scaled down to realistic values by dividing by the γ factor, described in section 4.2.3; this changes the absolute values of the potentials, but not the relative values. Two yellow bars on the bottom scale mark time periods when B_z was mostly or completely southward, and two yellow arrows mark peaks in the LFM CPCP corresponding to those time periods. For the first period, around DOY 86.2, the LFM CPCP peaked around 115 kV, while B0 at that time was around 45 kV, which means that the viscous potential was almost 40% of the LFM CPCP, with reconnection accounting for slightly over 60%. This is significant in that the viscous potential is often considered to be a small percentage of the CPCP when it is discussed in the literature – sometimes small enough to be ignored during magnetospherically active times. In the time period DOY 87.6-88.1 (also in Figure 4-8), the B0 run averages around 30-35 kV; the LFM CPCP peaks at around 135 kV, at which point the B0 run is around 35 kV - so the viscous potential is over 25% of the CPCP at that point.

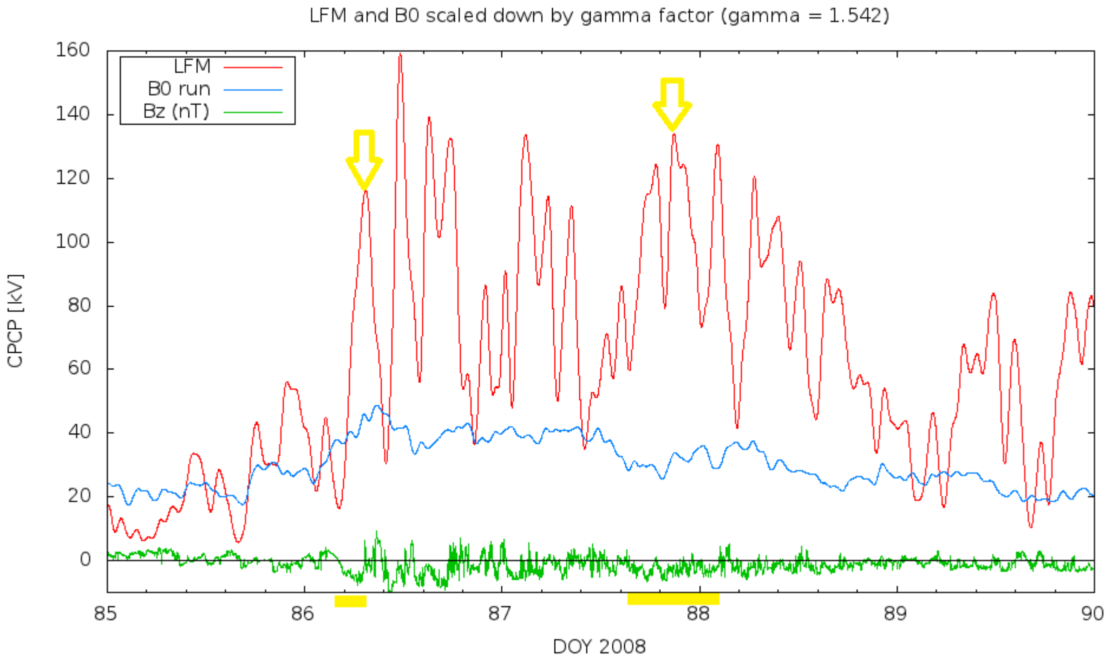

Figure 4-8. CPCP values for the full-IMF LFM and zero-IMF B0 runs for DOY 85-90.

Figure 4-9 shows a similar plot for another time period from the WHI, DOY 95-100, with DOY 95.7-95.8 highlighted. This period had one spike of northward B_z, but strong reconnection due to a large southward B_z component – almost -15 nT (which goes off the plot, since the scale only goes down to -10). The LFM CPCP is correspondingly large, reaching a peak of about 140 kV, which is one of the largest values recorded during the WHI. The B0 CPCP during this time is about 45 kV, which means that the viscous potential contributed about 1/3 of the CPCP.

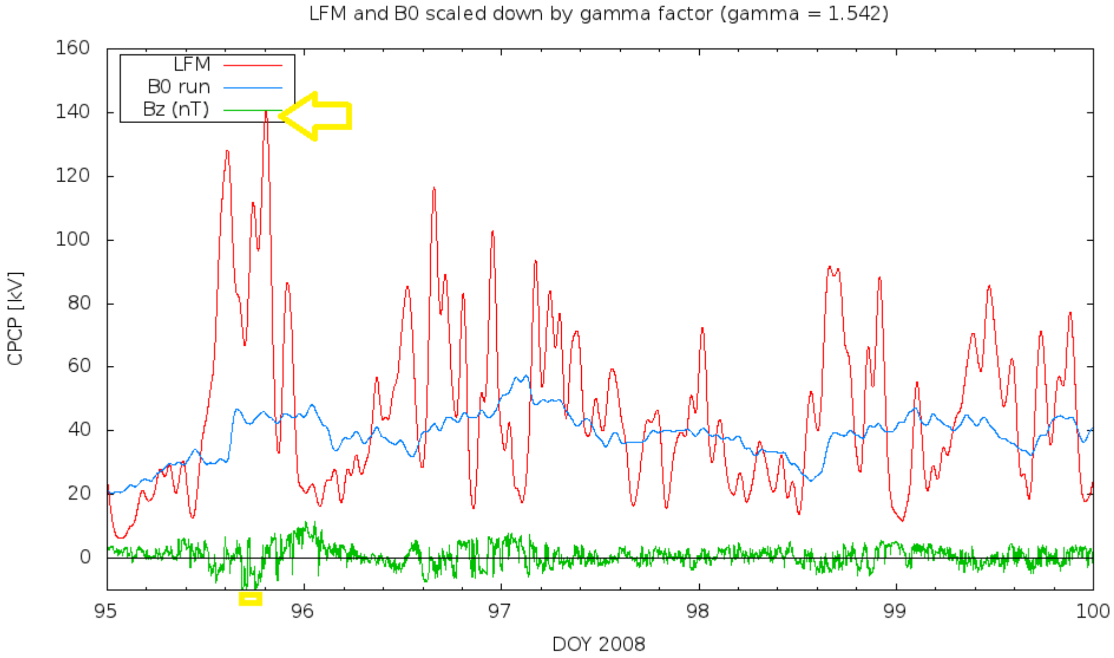

Figure 4-9. CPCP values for the full-IMF LFM and zero-IMF B0 runs for DOY 95-100.

These ratios of viscous potential to CPCP are not meant to represent the largest fraction that the viscous potential can take, or even typical values. They simply show that even for times when there is moderate-to-strong magnetospheric and ionospheric convection due to reconnection, the viscous interaction can still play a significant role in the composition of the CPCP.

4.2.3 Scaling the LFM potentials down to realistic values, using the Bruntz et al. formula

Since the CPCP for the B0 run gives the viscous potential, it can be compared to other models of the viscous potential, such as the Bruntz et al. viscous potential formula. Whereas the Bruntz et al. formula was derived from LFM runs using an ionospheric Pedersen conductance of 10 mhos, in order to produce realistic results, the

LFM and B0 runs used the empirical ionosphere with an F10.7 input value of 74 SFU, which was the average F10.7 for the WHI. The result is that the B0 ionospheric potentials are too high, such as the CPCP value > 200 kV on DOY 86 in Figure 1-1Figure 4-6, with only moderate driving. *Wiltberger et al.* [2012] argue that the reason for the high potentials in LFM is that the conductivity model is not producing high enough conductivity. Pedersen conductivity during the WHI typically fell in the range of 2-7 mhos, with larger values on the sunward part of the ionosphere and smaller values on the antisunward portion. Since the LFM model is known to produce realistic morphology in the ionospheric potential values, but the values are too high, we can posit that the B0 potentials will be of the form

$$\Phi_{\text{V-B0}} = \gamma\Phi_{\text{V-Bruntz}} = \gamma\mu n^{0.49}V^{1.33}$$

Equation 7

where γ is the factor by which the B0 potentials are too high and μ is the scaling term found in Section 3.5. We can modify Equation 7 to read:

$$\gamma = \mu n_0^{0.49}V_0^{1.33}/\Phi_0$$

Equation 8

where n_0, V_0 are input solar wind conditions and Φ_0 is the corresponding value taken from the B0 run. To avoid errors from Φ_0 values not being matched exactly to the driving n_0 and V_0, we chose eleven periods from the WHI when the input density and velocity, and the output ionospheric potential, were all fairly steady (e.g., DOY 89.0-89.5, 91.8-92.0, and 103.0-103.4).

Anticipating that we would also be using a similar technique to find a scaling factor to turn the *Newell et al.* [2008] coupling function into a predictive formula, $\Phi_{V\text{-}Newell} = \nu n^{1/2} V^2$ (Section 4.2.4), the question arose as to whether V should be V_{total} or V_x, which can differ somewhat. The *Bruntz et al.* [2012a] formula was derived using ideal solar wind data, where $V = V_x = V_{total}$, while the *Newell et al.* [2008] coupling function used $V = V_{total}$. In order to answer this question, we used both the Bruntz et al. and Newell et al. formulas, with both V_x and V_{total} as input, then plotted the results against the B0 CPCP values. The results are plotted in Figure 4-10, with a linear fit plotted for each of the four combinations. Note that preliminary values of $\gamma = 1.4$ and $\nu = 8.92\times10^{-5}$ were used in these calculations, but that multiplying a dataset by a constant does not affect the R^2 value, which tells how well the data match the line fit to them. Since that is the purpose of this part of the analysis, the specific values of γ and ν are unimportant.

It is also worth noting at this point that the Bruntz et al. and Newell et al. viscous potential formulae take solar wind input (from the OMNI data, plotted in Figure 4-4) and produce viscous potential values corresponding to that input. The OMNI data, however, represent the solar wind impinging on the point on the bow shock that is along the Sun-Earth line. The physical solar wind-magnetosphere-ionosphere system has a time delay from when the solar wind reaches the bow shock to when the ionosphere responds, due to the propagation time of the solar wind through the magnetosheath and the finite response time of the magnetosphere and ionosphere to changes in the solar wind. The full-IMF and zero-IMF LFM runs have this delay built-in, since they are modeling the physical system, but the Bruntz et al. and Newell et al. formulae do not.

Thus, in order for the LFM potentials to be compared to the Bruntz et al. and Newell et al. potentials, the formula-based potentials had to be time-shifted to match up with the LFM potentials. We did this by interpolating the zero-IMF CPCP values to every integer minute value in simulation time, to match the cadence and number of data points of the Bruntz et al. formula output, which has the integer-minute cadence of the OMNI data input. The formula value was then subtracted from the LFM value for each minute in the first 10 days of the WHI, that difference for each minute was squared, and those squared values were then averaged over the number of minutes involved, to give a single value for this time offset between the Bruntz et al. and LFM values (in this case, with zero offset). The Bruntz et al. timestep was then offset by an integral number of minutes, and the process repeated, for all 1-minute values from -100 to +100 minutes, to get a value for each offset. Those values were then examined to find a minimum, indicating the best correspondence between the Bruntz et al. values and the zero IMF LFM run. That value was then used to time shift the OMNI solar wind data that was input into the Bruntz et al. and Newell et al. formulae, so that the morphology of their output will be closely matched, temporally, to the morphology of the LFM output.

Looking at the results of the velocity comparisons in Figure 4-10, we see that for both the Bruntz et al. formula and the Newell et al. formula, V_x produced slightly better results (R^2 = 0.91) than V_{total} (R^2 = 0.88). Physically, it is not surprising that the velocity that correlates best with the viscous potential is the component that is flowing antisunward and perpendicular to the Earth’s dipole axis. It is also noteworthy that both formulas performed almost equally well, with their R^2 values only differing at the third decimal place and beyond (which are probably not significant). More qualitative results will be explored in Section 4.2.5.

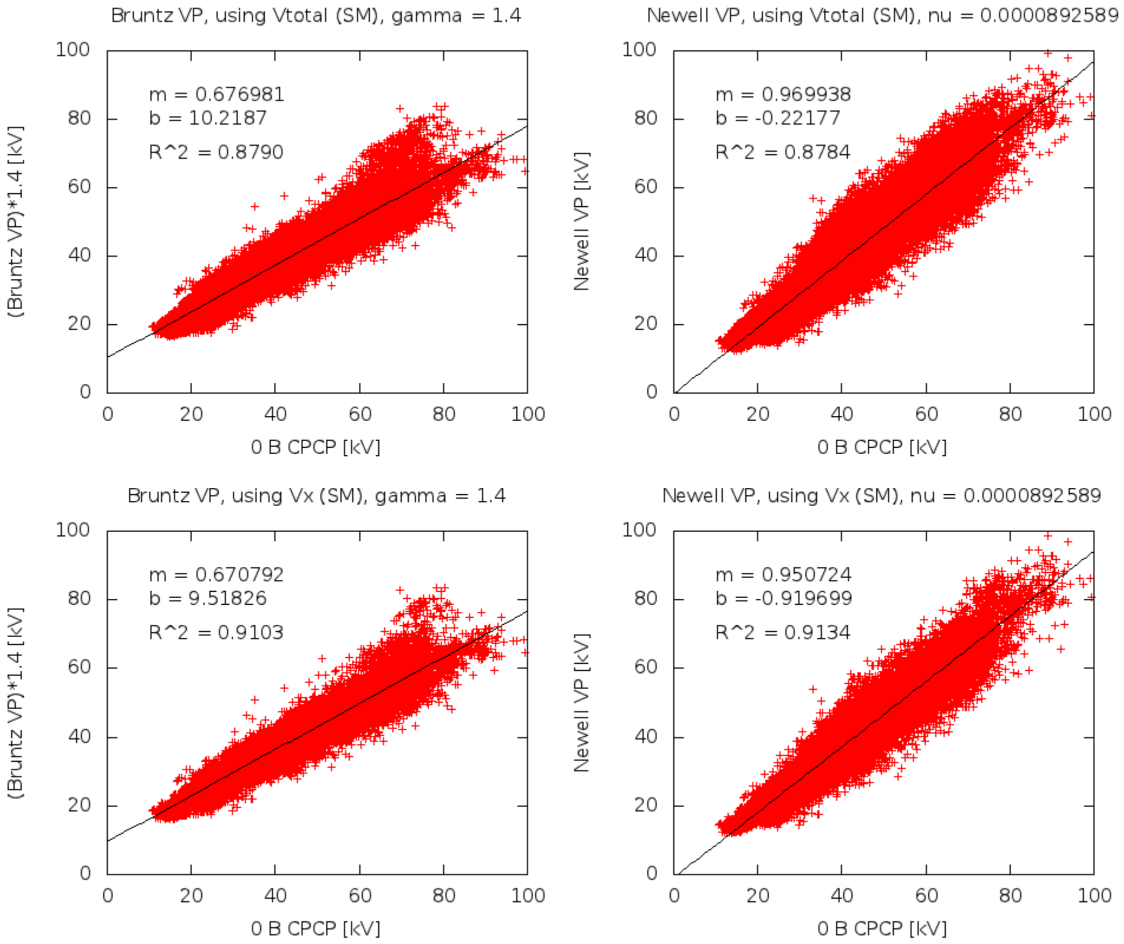

Figure 4-10. Results of the Bruntz et al. and Newell et al. equations, using V_x and V_{total} as input, plotted against the B0 CPCP. [From *Bruntz et al.*, 2012b.]

Having determined that V_x should be used in Equation 7 (and Equation 8), we solved for γ, using the average n, V_x, and Φ_{PC} from each of the 11 steady intervals to find 11 values of γ. These values ranged from 1.154 to 1.803. The 5 highest values corresponded to intervals during high speed streams (1.660-1.803) with the lowest 6 corresponding to slower solar wind values (1.154-1.616). Not wanting to use multiple γ

values, we took the simple average of the 11, yielding $\gamma = 1.542$. This is the average multiplicative factor by which the B0 run is overpredicting the CPCP, so any CPCP value from the B0 run divided by γ should be a realistic value, such as in Figure 4-8 and Figure 4-9.

4.2.4 Using the scaled zero IMF run to create a Newell et al. viscous potential formula

The *Newell et al.* [2008] viscous coupling function ($n^{1/2}V^2$) tells how the viscous interaction changes with changes in the solar wind density and velocity; it does not return an actual viscous potential value. If calibrated to a viscous potential value, however, the coupling function could be used to predict the viscous potential for any input solar wind density and velocity. Following the procedure used in Section 3.5, we can produce the equation

$$\Phi_V = (\Phi_{V0}/\gamma)(n/n_0)^{1/2}(V/V_0)^2 = \nu n^{1/2}V^2$$

Equation 9

Where Φ_{V0}, n_0, and V_0 are values from the B0 run and Φ_{V0} is scaled down by γ, to yield realistic potentials. In Equation 9, ν serves a comparable function to μ in the Bruntz et al. formula, though with a very different numerical value and even different units, due to differences in the density and velocity dependences. Using Φ_{V0}, n_0, and V_0 from the 11 steady intervals described in Section 4.2.3 yields 11 values of ν, ranging from 5.816×10^{-5} to 7.419×10^{-5}, with no clear trend with changing input density or velocity. With no reason to choose any value or weighting over another, we assigned ν the value of the average of the 11: $\nu = 6.393\times10^{-5}$. This results in an equation for predicting the viscous potential, using solar wind density and velocity as input, based on the *Newell et al.* [2008] viscous coupling function:

$$\Phi_{\text{V-Newell}} = \nu n^{1/2} V_x^{\,2} = (6.393\times 10^{-5}) n^{1/2} V_x^{\,2} \quad \text{(in kV)}$$

Equation 10

Where appropriate, we will refer to this as the “Newell et al. viscous potential formula.”

4.2.5 Comparing the Newell et al. and Bruntz et al. viscous potential formulas to the zero IMF run and each other

Using the above results, we have created a comparison plot, given in Figure 4-11 (which has been turned sideways, to enlarge the figure and give more detail). The panels in that figure are as follows: 1) Comparison of the unscaled B0 CPCP (i.e., not scaled down by γ) and the Bruntz et al. viscous potential; 2) Comparison of the scaled B0 CPCP and the Bruntz et al. viscous potential; 3) Comparison of the scaled B0 CPCP and the Newell et al. viscous potential; 4) Comparison of the Bruntz et al. and Newell et al. viscous potentials; and 5) Comparison of the scaled B0 CPCP and the Boyle et al. viscous potential. Note that the Boyle et al. viscous potential [*Boyle et al.*, 1997] is simply: $\Phi_{\text{V-Boyle}} = 10^{-4} V^2$, where $V = V_{total}$.

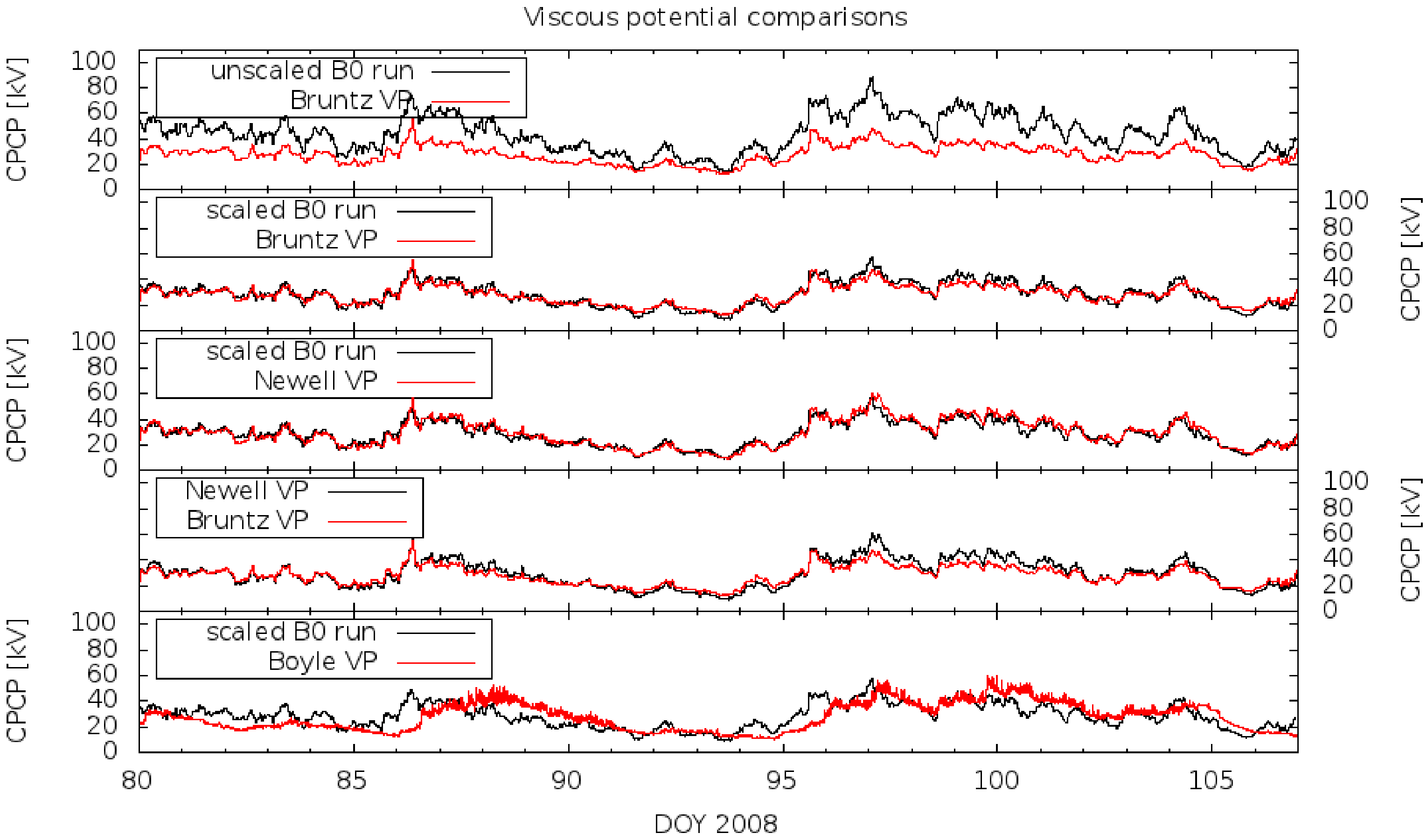

Figure 4-11. Comparisons of the B0 run CPCP, the Bruntz et al. viscous potential, the Newell et al. viscous potential, and the Boyle et al. viscous potential. [From *Bruntz et al.*, 2012b.]

Comparing the Bruntz et al. and the Newell et al. viscous potential formulae to the B0 run, we see that both do a remarkably good job of predicting the B0 CPCP values, which are composed of only the viscous potential. This close match in results is a little surprising, considering that the Bruntz et al. formula was created based entirely on steady-state polar cap potentials with a uniform-conductance ionosphere, not the constantly-changing values seen in the WHI run, with the empirical ionosphere.

The Bruntz et al. formula seems to slightly underpredict the B0 run during high speed streams, while the Newell et al. formula slightly overpredicts the B0 run during the same time periods. Plotting the two viscous potential formulae in the same panel, we see that the two give similar results for most of the WHI, but it is in fact during the periods of the highest solar wind velocity that the two predictions differ the most. This is easily explained by the form of the two equations, which have very different dependences on V (as was seen in Figure 4-2). The Boyle et al. formula captures the very general form of the B0 CPCP during the WHI, but misses most of the detailed structure, especially during the density enhancements associated with the CIRs (DOY 85-86 and 94-95). This is to be expected, since the Boyle et al. formula has no density dependence at all.

4.2.6 Comparing the scaled LFM potentials to an empirical model; implications for LFM

For the last analysis involving the WHI, we compared the full-solar wind LFM potentials to the Weimer05 model [*Weimer*, 2005], which is an empirical model that calculates various electrodynamic properties of the high-latitude ionosphere, including the CPCP. It is used as the background model for the Assimilative Mapping of Ionospheric Electrodynamics (AMIE) model [*Richmond and Kamide*, 1988; *Ridley and Kihn*, 2004], as well as serving as the high-latitude driver for several General Circulation Models (GCMs). Figure 4-12 shows two comparisons: The unscaled CPCP values from the full solar wind LFM run and the CPCP values from the Weimer05 model (also run from the full solar wind) in the first panel and the same comparison but with LFM scaled down by γ in the second panel.

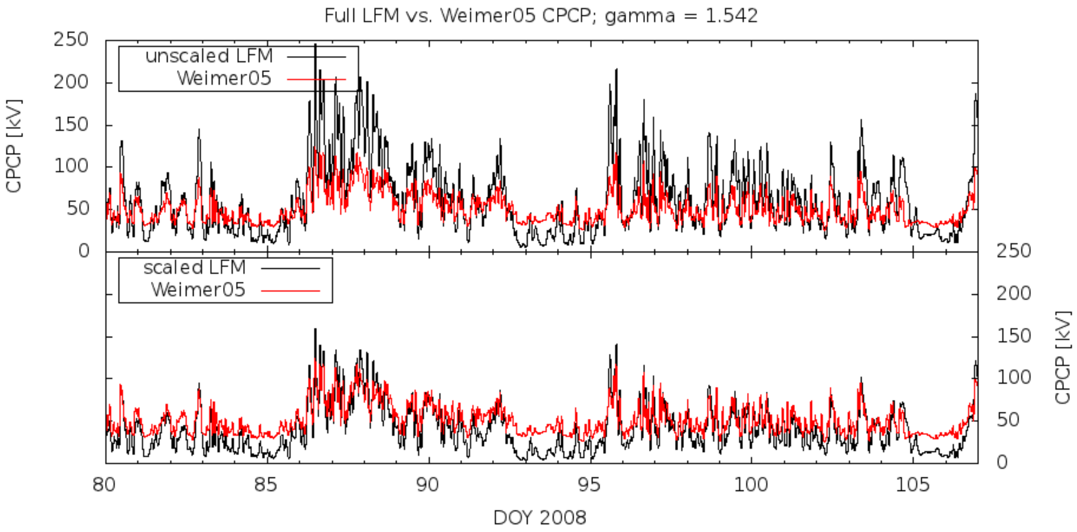

Figure 4-12. Comparison of the unscaled and scaled LFM run CPCP with the Weimer05 model CPCP. [From *Bruntz et al.*, 2012b.]

As was mentioned before, the unscaled LFM CPCP values tend to be too high, and are noticeably higher than the peaks of the more-realistic Weimer05 model output. Despite that, the LFM model still drops to noticeably lower minimum values than the lowest Weimer05 values. *Lopez et al.* [2012] explains this as a floor of ~25 kV in the

Weimer model, below which the model does not pass, regardless of the driving conditions. LFM has no set lowest CPCP values, but simply produces a CPCP value based on the solar wind and ionospheric conditions.

Since Weimer05 is an empirical model, it generally produces realistic CPCP values, and so, similar to the way we scaled the B0 run down to the levels of the realistic Bruntz et al. formula values using the γ factor, we might be able to scale the LFM values down to the Weimer05 level using γ. The results of this are plotted in the second panel of Figure 4-12. While the values do not match exactly, especially in the lower values of the LFM potentials, which were already lower than Weimer05, the higher CPCP values show remarkable agreement. This is significant in that γ was created to scale a viscous-only version of LFM run with an empirical ionosphere down to the range of the results of steady-state viscous-only LFM runs performed with constant-conductance ionosphere, yet it automatically scales the results of a viscous-plus-reconnection run down to the level of an empirical model that is in no way related to LFM. This implies that the γ factor is more than just a “fudge factor” for conversion between two specific data sets, but rather that it is correcting some deeper issue in the output of the LFM runs. We interpret this as support for the argument advanced by *Wiltberger et al.* [2012] that the ionospheric solver in LFM is producing conductances that are too low (due to insufficient auroral precipitation), and that that is the cause for the overly-high potentials in LFM. The γ factor corrects the effects of the too-low conductances, after the simulation is run.

CHAPTER 5

CONCLUSIONS AND FUTURE WORK

5.1 Conclusions

The solar wind flows out from the Sun constantly, in all directions, but not without significant variations in density, velocity, and magnetic field. As it flows past the Earth, the solar wind confines the Earth's magnetic field into a bubble, called the magnetosphere. The two main modes of energy transfer from the solar wind to the magnetosphere are magnetic reconnection and a viscous-like interaction. Studying solar wind-magnetosphere-ionosphere interactions directly is difficult, due to the low availability of direct measurements – the small number of satellites collecting data can only tell us about their nearby region of space and only at the time the satellite is there. Computer simulations, on the other hand, can observe the effects from any conditions that can be input, with whatever spatial and temporal resolution the simulation can run at.

We have used the Lyon-Fedder-Mobarry global 3-D magnetohydrodynamic (MHD) simulation to study the viscous interaction between the solar wind and Earth's magnetosphere. We ran the simulation with no interplanetary magnetic field (IMF), but a variety of solar wind velocity values (V_x = -300 km s^{-1} to -800 km s^{-1}, every 100 km s^{-1}) and density values (n = 1, 5, 8, 10, 15 cm^{-3}), as well as a variety of ionospheric conductivity values (Σ_P = 1, 2.5, 5, 7.5, 10, 12.5, 15, 20, 25, 30 mhos). With no IMF, there is no reconnection, and so only the viscous interaction couples the solar wind and magnetosphere, to create the cross-polar cap potential (Φ_{PC}), which is defined as the maximum potential across the polar ionosphere minus the minimum potential (regardless of their source). By running the simulation until it reaches steady-state, we can find the ionospheric potential due to the viscous interaction – the viscous potential (Φ_V). We found that the viscous potential in LFM changes with solar wind velocity as $V^{1.33}$, where V is in km s^{-1}; it changes with solar wind density as $n^{0.439}$, where n is in particles per cm^3 (cm^{-3}). Combining these results with a carefully-chosen reference LFM run, we produced a formula for the viscous potential in LFM: $\Phi_V = \mu n^{0.439} V^{1.33}$, where Φ_{VP} is in kV and $\mu = 0.00431$ (units omitted). Comparing the output of this "Bruntz et al. viscous potential formula" to the 30 runs performed with different velocity and density values shows that the formula is remarkably accurate at predicting the viscous potential in LFM. These runs were all performed with a constant ionospheric Σ_P = 10 mhos, which is known to produce realistic potentials. The runs performed with various Σ_P values (and identical, constant solar wind conditions) revealed that Φ_V varies inversely with Σ_P, as expected.

We compared the form of the Bruntz et al. formula to the *Newell et al.* [2008] study of a variety of viscous coupling functions. The form of the Bruntz et al. formula, $n^{0.439}V^{1.33}$, is closest in parameter space to the two best-performing coupling functions

($n^{1/2}V^2$, then $n^{1/3}V^2$) and lies at the edge of an untested region of parameter space, and so might perform better than these functions if tested against the same dataset.

We also looked at the viscous interaction during an LFM run using real solar wind data as input. The data used were from the Whole Heliosphere Interval (WHI), which was 20 March – 16 April, 2008 (DOY 80-107). The ionosphere used was the empirical model, with an F10.7 input of 74 solar flux units, which was the average for the WHI. Two runs were relevant to this work: one with the full solar wind input and one with the same solar wind, but all IMF components set to zero. The cross-polar cap potential (CPCP or Φ_{PC}) values for the zero-IMF run were larger than realistic values, which is common with LFM, so we scaled them down by a factor $\gamma = 1.54$, which was found by matching Φ_{PC} during 11 steady periods during the WHI to Φ_V from the Bruntz et al. formula, using the solar wind density and velocity values during those periods. We also used those same 11 periods to find a scaling factor to turn the Newell et al. viscous coupling function into a viscous potential formula: $\Phi_V = \nu n^{1/2}V^2$, where $\nu = 6.39\times10^{-5}$ (units omitted). Comparing the Bruntz et al. and Newell et al. viscous potential formulae to the zero-IMF run, we found that both did a very good job of predicting the zero-IMF (i.e., viscous) potentials, with one slightly overpredicting during high speed streams and the other slightly underpredicting, but both performing about equally well.

Comparing the zero-IMF and full-IMF runs, we showed that the viscous potential can be a significant fraction of the CPCP during southward *Bz*, even with strong driving and high CPCP values; it was not difficult to find Φ_V values that were

30-40% of the CPCP. We also showed that Φ_{PC} for the full-IMF run can drop lower than Φ_V (from the zero-IMF run) when the IMF is northward, which is consistent with very recent reports that northward B_z actually reduces the viscous interaction, and that for small values of northward B_z, $\Phi_{PC} = \Phi_V$, with no contribution from reconnection (Φ_R), which is different from the case for southward B_z, in which $\Phi_{PC} = \Phi_V + \Phi_R$.

Finally, we compared the full-IMF CPCP to the output of an empirical model, Weimer05. Like the zero-IMF run, the full-IMF run had to be scaled down by γ to produce realistic values. When compared to CPCP values from Weimer05, we found that the scaled-down LFM CPCP matched well, except for values below Weimer05's artificial "floor," since LFM has no such minimum CPCP value. This is noteworthy because the γ factor was derived from the Bruntz et al. formula (which used steady-state runs with no IMF and a constant-conductance ionosphere) and the zero-IMF LFM run (which used an empirical ionosphere), but neither dataset included effects from reconnection; whereas the full-IMF run included reconnection, and the Weimer05 model is completely unrelated to LFM – yet γ scaled the first to match the second. We take this as support for the idea that has been proposed, that the empirical ionosphere in LFM is producing conductances that are too low, and thus potentials that are too high; the γ factor was simply counteracting that effect.

5.2 Future Work

Some areas of future that might prove fruitful would include analyzing the LLBL in LFM, to try to calculate the viscous potential from the plasma flow. Since several studies have found viscous potentials in the LLBL in the range of 10 kV or less (sometimes much less), whereas ionospheric studies typically find several 10s of kV, it would be useful to find out if there is a mismatch between the two in the simulation, or if the issue is how the LLBL studies have been carried out (such as the location of the passes through the LLBL, as suggested by *Heikkila* [1986] and *Blomberg et al.* [2004]).

It would also be useful to study the effect of northward B_z on the viscous interaction, to try to parameterize the reduction on Φ_V as northward B_z increases, and perhaps look at the effect of east-west IMF (or verify that there is none). An investigation of the physical mechanism behind the observed reduction in Φ_V for northward B_z would also be very useful. (It is likely that some work will be done by Shree Bhattarai in both these areas in the next year, as part of his dissertation.)

It would be interesting to compare the Bruntz et al. and Newell et al. viscous potential formulae to direct Φ_{PC} measurements if some satellite passes could be found that match to time periods with nearly zero reconnection, if such time periods and passes can be found (such as in DMSP data). It would also be interesting to reexamine the data from some previous studies, such as *Reiff et al.* [1981] and *Boyle et al.* [1997], to see if removal of a viscous potential from the Φ_{PC} values examined in those studies produced data that extrapolated to $\Phi_{PC} = 0$ kV at zero IMF (i.e., removal of a viscous term leaves only a merging term, which goes to zero at zero IMF) and produces a better fit to the data (since the variation due to solar wind density in the viscous term is removed).

We would like to apply the methodology used in *Newell et al.* [2008], using the viscous coupling factor in the *Bruntz et al.* [2012a] formula, to see whether the results from LFM produce an improved accounting for magnetospheric variability. We plan to follow this line of inquiry as soon as the *Bruntz et al.* [2012b] paper has been published.

Finally, analyses of multiple satellite passes through the LLBL could be very useful. Passes at a variety of distances down the magnetopause could be analyzed for expected changes in the average LLBL plasma velocity and compared to LFM simulations for similar conditions. These satellites could also be used to look for viscous cells in the magnetotail, and if possible, calculate the potential across sunward and antisunward portions of the cells (by integrating **E·dl**). Again, these results could be compared to similar results in LFM.

REFERENCES

Axford, W. I., and C. O. Hines (1961), A unifying theory of high-latitude geophysical phenomena and geomagnetic storms, *Canad. J. Phys.*, *39*, pp. 1433-1464.

Bhattarai, S. K., R. E. Lopez, R. Bruntz, J. G. Lyon, and M. Wiltberger (2012), Simulation of the polar cap potential during periods with northward interplanetary magnetic field, *J. Geophys. Res.*, *117*, A04219, doi:10.1029/2011JA017143.

Blomberg, L. G., S. Eriksson, J.A. Cumnock, M. Yamauchi, J.H. Clemmons, G.T. Marklund, P.-A. Lindqvist, T. Karlsson, R. Lundin (2004), Solar wind-magnetosphere-ionosphere coupling: An event study based on Freja data, *J. Atmos. Sol. Terr. Phys.*, *66*, 375–380, doi:10.1016/j.jastp.2003.12.009.

Boyle, C., P. Reiff, and M. Hairston (1997), Empirical polar cap potentials, *J. Geophys. Res.*, *102*(A1), 111-125, doi:10.1029/96JA01742.

Bruntz, R., R. E. Lopez, M. Wiltberger, and J. G. Lyon (2012a), Investigation of the viscous potential using an MHD simulation, *J. Geophys. Res.*, *117*, A03214, doi:10.1029/2011JA017022.

Bruntz, R., R. E. Lopez, S. K. Bhattarai, K. H. Pham, Y. Deng, Y. Huang, M. Wiltberger, and J. G. Lyon (2012b), Investigating the viscous interaction and its role in generating the ionospheric potential during the Whole Heliosphere Interval, *J. Atmos. Sol. Terr. Phys.*, 10.1016/j.jastp.2012.03.016, in press.

Burke, W. J., M. C. Kelley, R. C. Sagalyn, M. Smiddy, and S. T. Lai (1979), Polar cap electric field structures with a northward interplanetary magnetic field, *Geophys. Res. Lett.*, *6*(1), 21–24, doi:10.1029/GL006i001p00021.

Burke, W., D. Weimer, and N. Maynard (1999), Geoeffective interplanetary scale sizes derived from regression analysis of polar cap potentials, *J. Geophys. Res.*, *104*(A5), 9989-9994, doi:10.1029/1999JA900031.

Claudepierre, S. G., S. R. Elkington, and M. Wiltberger (2008), Solar wind driving of magnetospheric ULF waves: Pulsations driven by velocity shear at the magnetopause, *J. Geophys. Res., 113*, A05218, doi:10.1029/2007JA012890.

Cowley, S. W. H. (1982), The causes of convection in the Earth's magnetosphere: A review of developments during the IMS, *Rev. Geophys.*, *20*(3), 531–565, doi:10.1029/RG020i003p00531.

Doyle, M. A., and W. J. Burke (1983), S3-2 measurements of the polar cap potential, *J. Geophys. Res.*, *88*(A11), 9125–9133, doi:10.1029/JA088iA11p09125.

Drake, K. A., R. A. Heelis, M. R. Hairston, and P. C. Anderson (2009), Electrostatic potential drop across the ionospheric signature of the low-latitude boundary layer, *J. Geophys. Res.*, *114*, A04215, doi:10.1029/2008JA013608.

Dungey, J. W. (1961), Interplanetary magnetic field and the auroral zones, *Phys. Rev. Lett.*, Vol. 6, pp. 47-48.

Eastman, T. E., E. W. Hones Jr., S. J. Bame, and J. R. Asbridge (1976), The magnetospheric boundary layer: Site of plasma, momentum and energy transfer from the magnetosheath into the magnetosphere, *Geophys. Res. Lett.*, *3*(11), 685-688, doi:10.1029/GL003i011p00685.

Fedder, J.A., S.P. Slinker, J.G. Lyon, R.D. Elphinstone (1995), Global numerical simulation of the growth phase and the expansion onset for substorm observed by Viking, *J. Geophys. Res.*,*100*(A10), 19083–19093, doi:10.1029/95JA01524.

Gibson, S.E., Kozyra, J.U., de Toma, G., Emery, B.A., Onsager, T., Thompson, B.J. (2009), If the Sun is so quiet, why is the Earth ringing? A comparison of two solar minimum intervals. *J. Geophys. Res.*, *114*, A09105. doi:10.1029/2009JA014342.

Goodrich, C. C., J. G. Lyon, M. Wiltberger, R. E. Lopez, and K. Papadopoulos (1998), An overview of the impact of the January 10–11 1997 magnetic cloud on the magnetosphere via global MHD simulation, *Geophys. Res. Lett.*, *25*(14), 2537–2540, doi:10.1029/98GL01159.

Hairston, M. R., R. A. Heelis, and F. J. Rich (1998), Analysis of the ionospheric cross polar cap potential drop using DMSP data during the National Space Weather Program study period, *J. Geophys. Res.*, *103*(A11), 26,337–26,347, doi:10.1029/97JA03241.

Hapgood, M., and M. Lockwood (1993), On the voltage and distance across the low latitude boundary layer, *Geophys. Res. Lett.*, *20*(2), 145–148, doi:10.1029/93GL00063.

Hasegawa, A. (1975), *Plasma Instabilities and Nonlinear Effects*, Springer, New York.

Heikkila, W. J. (1986), Comment on “Electric field evidence on the viscous interaction at the magnetopause”, by F. S. Mozer, *Geophys. Res. Lett.*, *13*(3), 233–234, doi:10.1029/GL013i003p00233.

Hughes, W. J., and M. K. Hudson (2004), Towards an integrated model of the space weather system, *J. Sol. Terr. Phys., 66*, 1241-1242, doi:10.1016/j.jastp.2004.06.001.

Kallenrode, M.-B. (2004), *Space Physics: An Introduction to Plasmas and Particles in the Heliosphere and Magnetospheres*, Springer, ISBN 3540206175.

Kivelson, M. G., C. T. Russell (editors) (1995), *Introduction to Space Physics*, Cambridge University Press, ISBN 0-521-45714-9.

Lopez, R.E. (1990), Magnetospheric Substorms, *Johns Hopkins APL Technical Digest*, *11*(3-4), 264-271.

Lopez, R. E., R. Bruntz, E. J. Mitchell, M. Wiltberger, J. G. Lyon, and V. G. Merkin (2010), Role of magnetosheath force balance in regulating the dayside reconnection potential, *J. Geophys. Res.*, *115*, A12216, doi:10.1029/2009JA014597.

Lopez, R. E., Bhattarai, S. K., Bruntz, R., Pham, K., Wiltberger, M., Lyon, J. G., Deng, Y., Huang, Y., (2012). The Role of Dayside Merging in Generating the Ionospheric Potential During the Whole Heliosphere Interval, submitted to *J. Atmos. Solar Terr. Phys.*, doi:10.1016/j.jastp.2012.03.001, in press.

Lyon, J. G., J. A. Fedder, and C. M. Mobarry (2004), The Lyon-Fedder-Mobarry (LFM) global MHD magnetospheric simulation code, *J. Atmos. Sol. Terr. Phys.*, *66*, 1333–1350, doi:10.1016/j.jastp.2004.03.020.

Merkin, V. G. and J. G. Lyon (2010), Effects of the low-latitude ionospheric boundary condition on the global magnetosphere, *J. Geophys. Res.*, *115*, A10202, doi:10.1029/2010JA015461.

Merkin, V., A. S. Sharma, K. Papadopoulos, G. Milikh, J. Lyon, and C. Goodrich (2005), Global MHD simulations of the strongly driven magnetosphere: Modeling of the transpolar potential saturation, *J. Geophys. Res.*, *110*, A09203, doi:10.1029/2004JA010993.

Mitchell, E. J., R. E. Lopez, R. J. Bruntz, M. Wiltberger, J. G. Lyon, R. C. Allen, S. J. Cockrell, and P. L. Whittlesey (2010), Saturation of transpolar potential for large Y component interplanetary magnetic field, *J. Geophys. Res.*, *115*, A06201, doi:10.1029/2009JA015119.

Mozer, F. S. (1984), Electric field evidence on the viscous interaction at the magnetopause, *Geophys. Res. Lett.*, *11*(2), 135–138, doi:10.1029/GL011i002p00135.

Mozer, F. S. (1986), Reply [to “Comment on “Electric field evidence on the viscous interaction at the magnetopause””], *Geophys. Res. Lett.*, *13*(3), 235–236, doi:10.1029/GL013i003p00235.

Mozer, F. S., H. Hayakawa, S. Kokubun, M. Nakamura, T. Okada, T. Yamamoto, and K. Tsuruda (1994), The morningside low-latitude boundary layer as determined from electric and magnetic field measurements on Geotail, *Geophys. Res. Lett.*, *21*(25), 2983–2986, doi:10.1029/94GL01296.

Newell, P. T., S. Wing, C.-I. Meng, and V. Sigillito (1991), The Auroral Oval Position, Structure, and Intensity of Precipitation from 1984 Onward: An Automated On-Line Data Base, *J. Geophys. Res.*, *96*(A4), 5877–5882, doi:10.1029/90JA02450.

Newell, P. T., T. Sotirelis, K. Liou, and F. J. Rich (2008), Pairs of solar wind - magnetosphere coupling functions: Combining a merging term with a viscous term works best, *J. Geophys. Res.*, *113*, A04218, doi:10.1029/2007JA012825.

Palmroth, M., Janhunen, P., Pulkkinen, T. I., Aksnes, A., Lu, G., Østgaard, N., Watermann, J., Reeves, G. D., and Germany, G. A.(2005), Assessment of ionospheric Joule heating by GUMICS-4 MHD simulation, AMIE, and satellite-based statistics: towards a synthesis, *Ann. Geophys.*, *23*, 2051-2068, doi:10.5194/angeo-23-2051-2005.

Powell, K., Roe, P., Linde, T., Gombosi, T., and De Zeeuw, D. L. (1999), A solution-adaptive upwind scheme for ideal magnetohydrodynamics, *J. Comp. Phys.*, *154*, 284-309.

Raeder, J., Larson, D., Li, W., Kepko, L., and Fuller-Rowell, T. (2008), OpenGGCM Simulations for the THEMIS Mission, *Space Sci. Rev.*, *141*, 535–555, doi:10.1007/s11214-008-9421-5.

Reiff, P., R. Spiro, and T. Hill (1981), Dependence of Polar Cap Potential Drop on Interplanetary Parameters, *J. Geophys. Res.*, *86*(A9), 7639-7648, doi:10.1029/JA086iA09p07639.

Richmond, A. D., and Y. Kamide (1988), Mapping Electrodynamic Features of the High-Latitude Ionosphere from Localized Observations: Technique, *J. Geophys. Res.*, *93*(A6), 5741–5759, doi:10.1029/JA093iA06p05741.

Ridley, A. J., and E. A. Kihn (2004), Polar cap index comparisons with AMIE cross polar cap potential, electric field, and polar cap area, *Geophys. Res. Lett.*, *31*, L07801, doi:10.1029/2003GL019113.

Russell, C. T., J. G. Luhmann, and G. Lu (2001), Nonlinear response of the polar ionosphere to large values of the interplanetary electric field, *J. Geophys. Res.*, *106*, 18,496–18,504.

Shepherd, S., and J. Ruohoniemi (2000), Electrostatic potential patterns in the high - latitude ionosphere constrained by SuperDARN measurements, *J. Geophys. Res.*, *105*(A10), 23005-23014, doi:10.1029/2000JA000171.

Shepherd, S. G., J. M. Ruohoniemi, and R. A. Greenwald (2003), Testing the Hill model of transpolar potential with Super Dual Auroral Radar Network observations, *Geophys. Res. Lett.*, *30*, 1002, doi:10.1029/2002GL015426.

Sibeck, D. G., R. E. Lopez, and E. C. Roelof (1991), Solar Wind Control of the Magnetopause Shape, Location, and Motion, *J. Geophys. Res.*, *96*(A4), 5489–5495, doi:10.1029/90JA02464.

Siscoe, G. L., G. M. Erickson, B.U.Ö. Sonnerup, N. C. Maynard, J. A. Schoendorf, K. D. Siebert, D. R. Weimer, W. W. White, and G. R. Wilson (2002), Hill model of transpolar potential saturation: Comparisons with MHD simulations, *J. Geophys. Res.*, *107*, A6, doi:10.1029/2001JA000109.

Sonnerup, B. U. Ö. (1980), Theory of the Low-Latitude Boundary Layer, *J. Geophys. Res.*, *85*(A5), 2017–2026, doi:10.1029/JA085iA05p02017.

Sonnerup, B., K. Siebert, W. White, D. Weimer, N. Maynard, J. Schoendorf, G. Wilson, G. Siscoe, and G. Erickson (2001), Simulations of the magnetosphere for zero interplanetary magnetic field: The ground state, *J. Geophys. Res.*, *106*(A12), 29419-29434, doi:10.1029/2001JA000124.

Stern, D. P. (1996), A brief history of magnetospheric physics during the space age, *Rev. Geophys.*, *34*, 1-37.

Sundberg, K. Å. T., L. G. Blomberg, and J. A. Cumnock (2008), Statistical analysis of the sources of the cross-polar potential for southward IMF, based on particle precipitation characteristics, *Geophys. Res. Lett.*, *35*, L08103, doi:10.1029/2008GL033383.

Sundberg, K. A˚. T., L. G. Blomberg, and J. A. Cumnock (2009), Properties of the boundary layer potential for northward interplanetary magnetic field, *Geophys. Res. Lett.*, *36*, L11104, doi:10.1029/ 2009GL038625.

Vasyliunas, V. M. (2001), Electric field and plasma flow: What drives what?, *Geophys. Res. Lett.*, *28*(11), 2177–2180, doi:10.1029/2001GL013014.

Wang, W., Wiltberger, M., Burns, A. G., Solomon, S., Killeen, T. I. (2004), Initial results from the center for integrated space weather modeling coupled magnetosphere ionosphere thermosphere model: Ionospheric and thermospheric responses. *J. Atmos. Solar Terr. Phys.*, *66*, 1425-1441, doi:10.1016/j.jastp.2004.04.008.

Watanabe, M., K. Kabin, G. J. Sofko, R. Rankin, T. I. Gombosi, and A. J. Ridley (2010), pole tilt effects on the magnetosphere - ionosphere convection system during interplanetary magnetic field BY - dominated periods: MHD modeling, *J. Geophys. Res.*, *115*, A07218, doi:10.1029/2009JA014910.

Weimer, D. R. (2005), Improved ionospheric electrodynamic models and application to calculating Joule heating rates, *J. Geophys. Res.*, *110*, A05306, doi:10.1029/2004JA010884.

Wilder, F. D., C. R. Clauer, J. B. H. Baker, E. P. Cousins, and M. R. Hairston (2011), The nonlinear response of the polar cap potential under southward IMF: A statistical view, *J. Geophys. Res.*, *116*, A12229, doi:10.1029/2011JA016924.

Wiltberger, M., T. Pulkkinen, J. Lyon, and C. Goodrich (2000), MHD simulation of the magnetotail during the December 10, 1996, substorm, *J. Geophys. Res.*, *105*(A12), 27649-27663, doi:10.1029/1999JA000251.

Wiltberger, M., Wang, W., Burns, A., Solomon, S., Lyon, J. G., Goodrich, C. C. (2004), Initial results from the coupled magnetosphere ionosphere thermosphere model: Magnetospheric and ionospheric responses. *J. Atmos. Solar Terr. Phys. 66*, 1411-1423, doi:10.1016/j.jastp.2004.03.026.

Wiltberger, M., R. S. Weigel, W. Lotko, and J. A. Fedder (2009), Modeling seasonal variations of auroral particle precipitation in a global-scale magnetosphere-ionosphere simulation, *J. Geophys. Res.*, *114*, A01204, doi:10.1029/2008JA013108.

Wiltberger, M., L. Qain, C. -L. Huang, W. Wang, R. E. Lopez, A. G. Burns, S. C. Solomon, Y. Deng, Y. Huang (2012), CMIT study of CR2060 and 2068 comparing L1 and MAS solar wind drivers, *J. Sol. Terr. Phys.*, doi:10.1016/j.jastp.2012.01.005.

Wygant, J., R. Torbert, and F. Mozer (1983), Comparison of S3−3 Polar Cap Potential Drops with the Interplanetary Magnetic Field and Models of Magnetopause Reconnection, *J. Geophys. Res.*, *88*(A7), 5727-5735, doi:10.1029/JA088iA07p05727.

BIOGRAPHICAL INFORMATION

Robert Bruntz received his Bachelor’s degree in 1999 from the University of Texas at El Paso (UTEP), majoring in Linguistics with a minor in Physics. He immediately entered graduate school, pursuing his Master’s in Physics. He began working for Dr. Ramon E. Lopez as a Teaching and Research Assistant in the summer of 2000, initially studying Physics Education, but soon switching to Space Physics. He soon became the unofficial computer wrangler for the Lopez group, and in Feb. 2004 became the official Lab Manager, in preparation for the group’s move to the Florida Institute of Technology in July of 2004. He finished writing his Master’s thesis at Florida Tech and returned to UTEP in May of 2005 to (successfully) defend his thesis, entitled “Predicting ring current development using global MHD simulations of geomagnetic storms.”

He worked as the Lab Manager for Dr. Lopez at Florida Tech from August 2004 through July 2007, at which point the group moved to the University of Texas at Arlington (UTA). During that time at Florida Tech, he took a few graduate courses and was involved in some research, but was mostly involved in running the lab and working with students in the group, including training them in various technological and scientific systems, and overseeing undergraduate research groups.

As Lab Manager at UT Arlington, he oversaw renovation of the new lab for the Lopez Research Group and rebuilt the computer and visualization systems for the group. He continued to take graduate courses intermittently (though not enrolled in a degree-seeking program) and began to participate more in specific research programs within the group, while still serving as a mentor for undergraduate researcher groups.

In the spring of 2011, he switched from Lab Manager to full-time PhD student. He successfully defended his dissertation, entitled “A study of the viscous interaction between the solar wind and Earth's magnetosphere using an MHD simulation,” on 17 April 2012 and graduated with his PhD on 13 May 2012.

Robert began working with the Center for Integrated Space Weather Modeling (CISM) as an early graduate student, under the leadership of Dr. Lopez, who was a co-PI on CISM, and kept working with CISM as the Lab Manager for the Lopez group. He is now looking for other sources of funding to continue Space Physics research. He is particularly interested in various methods of studying the viscous interaction and its contribution to ionospheric dynamics, with the goal of quantifying its contribution and minimizing the uncertainty in that contribution, in order to improve understanding of related phenomena. He would like to do more coordinated work between satellite measurements and MHD simulations.

His immediate post-graduation plans are to find a Post-doc position, or maybe two in succession, with NASA being one preferred source. He would then like to find a more permanent position in academia (but continuing research) or as a full-time researcher. Someday, one way or another, he still plans to make it into space.